

# Economic Geology

## Fluid Evolution and Skarn Mineralization in the Bingham Canyon Cu-Mo-Au Deposit, Utah, USA

--Manuscript Draft--

<b>Manuscript Number:</b>	SEG-D-18-00133R2
<b>Full Title:</b>	Fluid Evolution and Skarn Mineralization in the Bingham Canyon Cu-Mo-Au Deposit, Utah, USA
<b>Article Type:</b>	Regular Paper
<b>Corresponding Author:</b>	Katerina Schlöglova, Dr. Albert-Ludwigs-Universität Freiburg Freiburg im Breisgau, Baden-Württemberg GERMANY
<b>Corresponding Author Secondary Information:</b>	
<b>Corresponding Author's Institution:</b>	Albert-Ludwigs-Universität Freiburg
<b>Corresponding Author's Secondary Institution:</b>	
<b>First Author:</b>	Katerina Schlöglova, Dr.
<b>First Author Secondary Information:</b>	
<b>Order of Authors:</b>	Katerina Schlöglova, Dr.  Oscar Laurent  Markus Wölle  Christoph A. Heinrich
<b>Order of Authors Secondary Information:</b>	
<b>Abstract:</b>	The Bingham Canyon Cu-Mo-Au deposit hosts porphyry-style and skarn ores. In this study, we combine fluid inclusion petrography and microthermometry with laser ablation-inductively coupled plasma mass spectrometry (LA-ICP-MS) to constrain evolution and chemistry of the skarn-forming fluids. Alteration of impure limestones by magmatic-hydrothermal fluids, related to the emplacement of porphyry intrusions, resulted in the formation of calc-silicate mineral assemblages. The skarn-forming process includes early wollastonite and pyroxene formation (recrystallizing from Fe-poor to Fe-rich diopside) and replacement of wollastonite by several generations of garnet (grossular to andradite). The anhydrous skarn mineralization peaked by the introduction of quartz, sulfides and calcite. Pyroxene, garnet and quartz, formed during the main stage of skarn alteration preserve coeval fluid inclusions of three types: intermediate-density, brine and vapor inclusions. Identical salinities, formation temperatures and trace element content, recorded in respective fluid inclusions types in all three skarn host minerals suggest that the fluid inclusions did not undergo severe post-entrapment modification. Initial magmatic single-phase fluid of intermediate density (~0.6 g·cm <sup>-3</sup> , 10–20 wt. % NaCleq), preserved in the deep barren center of the deposit, formed above 550 °C and 800 bar. Upon cooling and decompression below ~400 °C and ~200 bar, the fluid separated into highly saline brine (32–42 wt. % NaCleq) and low-density, low-salinity vapor (~0.2 g·cm <sup>-3</sup> , 2–7 wt. % NaCleq), both of which were entrapped in the upper parts of the deposit. These fluids predate the major sulfide mineralization in the skarns. They share similar P-T path and trace element chemistry with the fluids found in the porphyry quartz stockwork, with the notable exception of lower S and ore metal (Ag, Au, Cu and Mo) contents. Ore metal grades are, however, comparable or higher in the skarns, when compared to the porphyry lithologies. This inverse correlation indicates that sulfide precipitation in the skarns was more effective, aided by pH neutralization of the magmatic fluid, in destabilizing the metal complexes. Brittle behavior of the skarns and changes in hydrology facilitated high density veining and intense fluid-rock reaction.



**Economic Geology**

**Institute of Geochemistry and Petrology, ETH Zurich**

Fluids and Mineral Resources Group  
Clausiusstrasse 25, CH-8092 Zurich  
[www.orefluids.ethz.ch](http://www.orefluids.ethz.ch)

Zurich, July 03, 2018

Dear Dr. Meinert,

herewith, we submit the manuscript

**"Fluid Evolution and Skarn Mineralization in the Bingham Canyon Cu-Mo-Au Deposit, Utah, USA"**

by Katerina Schloglova, Oscar Laurent, Markus Walle, and Christoph A. Heinrich asking you to consider it for publication in *Economic Geology*.

Skarns related to acidic magmatism and porphyry-style mineralization are world's important resources of copper, gold, molybdenum, silver, lead, and zinc. Even though the skarn mineralization process has been well-studied and described in the scientific literature, the physical and chemical properties of skarn-forming fluids are still largely unknown.

We constrain the evolution and chemistry of the skarn-forming fluids in the Bingham Canyon Cu-Mo-Au deposit in Utah, USA. Careful petrography, microthermometry, and laser-ablation inductively-coupled-plasma mass-spectrometry (LA-ICP-MS) were conducted on fluid inclusions entrapped simultaneously in quartz, garnet and pyroxene. These minerals are representative of the prograde skarn assemblage formed prior to major sulfide precipitation in the Bingham Canyon.

Coexistence of high-temperature magmatic fluid in the various skarn minerals allowed us to assess the degree of preservation of these fluid inclusions. We can rule out any post-entrapment modification of the inclusions and therefore provide unique data on the chemical composition and metal budget of the mineralizing fluids. Moreover, our results can be directly compared to fluids preserved in the highly-mineralized porphyry quartz stockwork, studied extensively by previous authors, to clarify the fluid evolution and mineralization in the two contrasting host-rock environments.

This study brings unique analytical data from a world class mineral deposit and introduces a novel approach to study of fluid inclusions in complex minerals. We believe that this paper will be of interest to the diverse readership of *Economic Geology*.

Potential reviewers with complementary expertise include:

Marco T. Einaudi (professor emeritus, Stanford) [mweinaudi@gmail.com](mailto:mweinaudi@gmail.com)  
Iain M. Samson (professor, University of Windsor) [ims@uwindsor.ca](mailto:ims@uwindsor.ca)  
Peter Kodera (associate professor, Comenius University in Bratislava) [peter.kodera@uniba.sk](mailto:peter.kodera@uniba.sk)  
David Lentz (professor, University of New Brunswick) [dlentz@unb.ca](mailto:dlentz@unb.ca)  
Mark D. Barton (professor, University of Arizona) [barton@geo.arizona.edu](mailto:barton@geo.arizona.edu)  
Lawrence D. Meinert (deputy director, USGS) [lmeinert@usgs.gov](mailto:lmeinert@usgs.gov)

Yours sincerely,  
Katerina Schloglova and co-authors

Zurich, August 28, 2018

Dear Dr. Meinert,

herewith we would like to re-submit the manuscript entitled

**"Fluid Evolution and Skarn Mineralization in the Bingham Canyon Cu-Mo-Au Deposit, Utah, USA"**

by Katerina Schlöglova, Oscar Laurent, Markus Wölle, and Christoph A. Heinrich and ask you to consider it for publication in *Economic Geology*.

We would like to thank you for your initial comments and suggestions for improvement of the manuscript. Below, please see the detailed response to your comments.

**COMMENTS:** Dear Katerina, your manuscript entitled, "Fluid Evolution and Skarn Mineralization in the Bingham Canyon Cu-Mo-Au Deposit, Utah, USA" has been received. This looks to be an interesting study of skarn-forming fluids and has the potential to be the best done to date. However, there are some things that need to be attended to before this can be sent out for review. I don't want reviewers to get distracted from the science by errant references and mineralogical problems. For example, not citing and apparently being unaware of a 2003 publication (see below) with similar conclusions to the present, albeit more detailed study, does not give the reader confidence in your scholarship.

Although generally well written, there are quite a few English grammar problems that would be caught during review by a native English speaker. For example, "The potential of skarn ores....is at 20 Mt", "Only with discovery of Cu-bearing porphyries in the center of the district and development of new mining methods and mineral flotation did production of Cu and Mo start in 1906", "We thank to Marcel Guillong". Some of these are not only awkward but in fact incorrect. For example, I suspect that Mo was not produced in 1906.

**ANSWER:** The above-mentioned inconsistencies were corrected (see e.g. P2 L12, P2 L20, P24 L37). Entire text of the manuscript was also re-read to check for any additional inconsistencies, grammar and typing errors.

**COMMENTS:** The skarn mineralogy and textural relations are not well explained. For example, pyroxene and garnet are minerals and diopside and andradite are specific compositional ranges of those minerals. All diopside is pyroxene but not all pyroxene is diopside. You have not used these terms consistently and correctly. Go back and read the 100th Anniversary Volume review paper to see how to study and describe skarns properly. The compositional variation usually is described in terms of the Fe end member, i.e. Hd38 or Ad82 and illustrated on ternary plots of the relevant end members. Alternatively, you could list the complete composition, which for one of your analyses would be Di60.4 Hd38.2 Jo1.4. All of your compositions fall well within the expected compositional range for Cu skarns and the paper would be far more useful if it was consistent with normal skarn terminology. You should be particularly careful about assuming, as you often do, that minerals that occur together are coeval. You use coeval a lot and I suspect that few of them are. Please review the meaning of assemblage versus association and using genetic terms carefully.

**ANSWER:** We have identified and evaluated all occurrences of mineral and end-member names in the manuscript and illustrations. We appreciate that mineral names are used in two different contexts: (1) as petrographic or paragenetic information, and (2) as host identifiers for fluid inclusions. During

revision, we have followed the editorial advice and unified the mineral names (e.g. garnet vs. andradite and pyroxene vs. diopside) throughout the manuscript, including the figures and tables. After careful consideration and for retaining fluency of the text, we have decided to use the mineral group names (i.e., garnet or pyroxene) for general rock description and petrography. Where the context requires further specification or information – such as chemical variation of the minerals during protracted skarn formation or for linking fluid inclusion petrography to specific mineral varieties – we added the names of the actual mineral end-members (e.g. andradite and diopside, or with additional qualifiers such as Al-poor and Al-rich andradite). The compositional variation of garnet and pyroxene (e.g.  $\text{Adr}_{23}\text{Grs}_{77}$  and  $\text{Di}_{98}\text{Hd}_{02}$ ) is extensively used in the chapter “Skarn mineral paragenesis” (P11 L35 through P12 L21).

**COMMENTS:** I have made a few notes below on the first couple of pages to give you some guidance, but have not gone through this in detail. I think a rewrite prior to review will get this to the finish line more quickly than sending it out for review as is.

P2 L15 There are several statements that need to be refined with proper citations. For example, relative to the amount of skarn versus porphyry ore, you need to read and cite: Simon M. Jowitt, Gavin M. Mudd, Zhehan Weng, 2013, HIDDEN MINERAL DEPOSITS IN Cu-DOMINATED PORPHYRY-SKARN SYSTEMS: HOW RESOURCE REPORTING CAN OCCLUDE IMPORTANT MINERALIZATION TYPES WITHIN MINING CAMPS: *Economic Geology*, v108 (5): 1185-1193.

ANSWER: We found the recommended article rather interesting and decided to add the reference to our manuscript (P2 L16). However, we wish to stress that the amount of skarn ores contributing to the general exploitable resource at Bingham Canyon is based on a long-term resource estimate done by Rio Tinto (Kennecott Utah Copper Corp.) which we do not intend to criticize or re-assess on our own.

**COMMENTS:** P2 L18 What is galenite? Do you mean galena?

P2 L47 What are concentric sulfide veins? This geometry would be circular and no such veins have been documented.

ANSWER: We have corrected “gallenite” to galena (P2 L18). The term “concentric” sulfide vein has been removed (P2 L45).

**COMMENTS:** P3 L23 This is not the place for nor is this a useful review of the skarn literature. The listed references are a strange and incomplete list. Why list a relatively obscure 1977 reference as some sort of starting point? There are far earlier references. And why stop at 1992? There are much more current publications. Again, this is not the place for and you have not done a good job of summarizing the skarn literature. You should simply cite the most current skarn review paper (100th Anniversary Volume of *Economic Geology*) and move on to your study. The same is true for the citations about porphyries, carbonate replacement deposits, etc. Such literature reviews and citations may be appropriate for a thesis but not for a scientific publication. Remove all of this.

P3 L41 Again, this summary of fluid inclusions in skarn deposits is not adequate. This is not the place to try to review the literature (and you have not done a good job). For example in the statement “phase separation, high formation temperatures and salinities decreasing with distance from the source” you have omitted the two most relevant studies (phase separation - Meinert, L. D., Hedenquist, J.W., Satoh, H., and Matsuhisa, Y., 2003, Formation of Anhydrous and Hydrous Skarn in Cu-Au Ore Deposits by Magmatic Fluids: *Economic Geology*, v. 98, p. 147-156 and temperature gradients - Meinert, L.D., 1987, Skarn zonation and fluid evolution in the Groundhog Mine, Central Mining District, New Mexico, *Economic Geology*, v. 82, 523-545.) The point is that in a study of a specific deposit you should not be attempting to review the world literature. That may be appropriate for a thesis, but not the present

study of Bingham skarn fluids. Simply cite a few examples (a useful rule of thumb is: first, best, and most recent) and then move on to your study.

ANSWER: We have reduced the introduction with emphasis on objectives and relevant aspects (see P3 L12-47). The review of skarn and porphyry literature was shortened as it is not the main subject of our study. We also incorporated some of the above-mentioned references (e.g. Meinert et al., 2003) in the review of the skarn-forming fluids where appropriate (e.g. P3 L32).

The entire manuscript was proof-read by the authors and another independent scientist to assure internal consistency of the text, graphics and references, as well as to eliminate remaining linguistic issues. The authors also consulted recent articles published in *Economic Geology* to compare our technical presentation with current journal style.

We kindly ask you to consider the manuscript for review and eventual publication in *Economic Geology*.

Best regards,  
Katerina Schläglova and co-authors

# Fluid Evolution and Skarn Mineralization in the Bingham Canyon Cu-Mo-Au Deposit, Utah, USA

Katerina Schloglova<sup>1,†,\*</sup>, Oscar Laurent<sup>1</sup>, Markus Wölle<sup>1,\*\*</sup> and Christoph A. Heinrich<sup>1,2</sup>

<sup>1</sup>*Institute of Geochemistry and Petrology, ETH Zurich, Clausiusstrasse 25, 8092 Zurich, Switzerland*

<sup>2</sup>*Faculty of Mathematics and Natural Sciences, University of Zurich, 8093 Zurich, Switzerland*

†corresponding author: e-mail, schloglo@gmail.com

\*Current address: Institute of Earth and Environmental Sciences, University of Freiburg, Albertstrasse 23b, 79104 Freiburg im Breisgau, Germany

\*\*Current address: CCCS, Memorial University of Newfoundland, St. John's, NL A1C 5S7, Canada

## Abstract

The Bingham Canyon Cu-Mo-Au deposit hosts porphyry-style and skarn ores. In this study, we combine fluid inclusion petrography and microthermometry with laser ablation-inductively coupled plasma mass spectrometry (LA-ICP-MS) to constrain evolution and chemistry of the skarn-forming fluids. Alteration of impure limestones by magmatic-hydrothermal fluids, related to the emplacement of porphyry intrusions, resulted in the formation of calc-silicate mineral assemblages. The skarn-forming process includes early wollastonite and pyroxene formation (recrystallizing from Fe-poor to Fe-rich diopside) and replacement of wollastonite by several generations of garnet (grossular to andradite). The anhydrous skarn mineralization peaked by the introduction of quartz, sulfides and calcite. Pyroxene, garnet and quartz, formed during the main stage of skarn alteration preserve coeval fluid inclusions of three types: intermediate-density, brine and vapor inclusions. Identical salinities, formation temperatures and trace element content, recorded in respective fluid inclusions types in all three skarn host minerals suggest that the fluid inclusions did not undergo severe post-entrapment modification. Initial magmatic single-phase fluid of intermediate density ( $\sim 0.6 \text{ g}\cdot\text{cm}^{-3}$ , 10–20 wt. % NaCl<sub>eq</sub>), preserved in the deep barren center of the deposit, formed above 550 °C and 800 bar. Upon cooling and decompression below ~400 °C and ~200 bar, the fluid separated into highly saline brine (32–42 wt. % NaCl<sub>eq</sub>) and low-density, low-salinity vapor ( $\sim 0.2 \text{ g}\cdot\text{cm}^{-3}$ , 2–7 wt. % NaCl<sub>eq</sub>), both of which were entrapped in the upper parts of the deposit. These fluids predate the major sulfide mineralization in the skarns. They share similar *P-T* path and trace element chemistry with the fluids found in the porphyry quartz stockwork, with the notable exception of lower S and ore metal (Ag, Au, Cu and Mo) contents. Ore metal grades are, however, comparable or higher in the skarns, when compared to the porphyry lithologies. This inverse correlation indicates that sulfide precipitation in the skarns was more effective, aided by pH neutralization of the magmatic fluid, in destabilizing the metal complexes. Brittle behavior of the skarns and changes in hydrology facilitated high density veining and intense fluid-rock reaction.

## Introduction

Bingham Canyon copper mine, located 40 km southwest of Salt Lake City (Utah, USA), is a world class porphyry copper deposit, which has produced over 2.8 billion tons of ore (Krahulec, 2010). The mine has been operating since 1906 and annually yields over 230 kt Cu from an average grade of 0.74 %, 12 t Au @ 0.4458 g/t, 100 t Ag @ 3.29 g/t, and 15 kt Mo @ 0.035 % (Porter et al., 2012; Rio Tinto 2017 Annual report). The economic potential of skarn ores, replacing carbonate-rich sedimentary rocks enclosed in and adjacent to intrusive rocks, is at 20 Mt @ 3.65 % Cu, 1.62 g/t Au and 20.95 g/t Ag; i.e. the skarns contribute ca. 10 % to the bulk mineable metal resource of the Bingham Canyon deposit (Krahulec, 2010; Jowitt et al., 2013). The deposit is part of the polymetallic Bingham mining district discovered in 1863 and exploited initially for Ag-bearing galena-sphalerite ores and placer gold (Boutwell, 1905; Johnson, 1973). Production of Cu started only after discovery of Cu-bearing porphyries in the center of the district and development of new mining methods and mineral flotation (De Kalb, 1909; Beeson, 1917). The Bingham mining district is one of the best-studied ore districts worldwide: from early publications prior to opening of the mines (Boutwell, 1905; Butler et al., 1920) to early work on sedimentary hosted ores (Hunt, 1924; Lindgren, 1924; Winchell, 1924; Stacey et al., 1967; Rubright and Hart, 1968; Field and Moore, 1971), to studies of the porphyry ores (James et al., 1961a; Phillips et al., 1998). The general geology of the district and overviews of the deposit types are detailed in a Special Issue of Economic Geology no. 73 (Einaudi et al., 1978), in Babcock et al. (1995), and in SEG Guidebook no. 29 (John and Ballantyne, 1997). The mining history of the district is well summarized by Smith (1975), James (1978) and Krahulec (2010).

The role of magmatic-hydrothermal processes in the formation of the porphyry type mineralization at Bingham is supported by numerous studies of fluid inclusions, including their composition (Roedder, 1971; Nash, 1976; John, 1989; Heinrich et al., 1999; Landtwing et al., 2002; Redmond et al., 2004; Landtwing et al., 2010; Seo et al., 2012) and isotopic signatures (Sheppard et al., 1971; Irwin and Roedder, 1995; Kendrick et al., 2001a; Kendrick et al., 2001b; Fekete et al., 2016). Porphyry Cu-Mo-Au mineralization requires exsolution of fluids from a magma chamber beneath the subvolcanic intrusions (Dilles, 1987; Redmond et al., 2004; Proffett, 2009; Steinberger et al., 2013). Precipitation of sulfide veins was driven by cooling and fluid-rock interaction (Hemley and Hunt, 1992; Inan and Einaudi, 2002; Redmond et al., 2004; Landtwing et al., 2005; Gruen et al., 2010; Weis et al., 2012). Fluid inclusion studies (Roedder, 1971; Redmond et al., 2004; Landtwing et al., 2010) recognized several stages of vein formation and major types of fluids. A single-phase fluid of intermediate density and rather low salinity ( $\sim 0.6 \text{ g}\cdot\text{cm}^{-3}$ , 7 wt. %  $\text{NaCl}_{\text{eq}}$ ) with minor amounts of  $\text{CO}_2$  is present mostly in the deeper parts of the deposit and is associated with early barren quartz veins. The early veining stage also bears abundant, spatially co-existing high-salinity brine (38–50 wt. %  $\text{NaCl}_{\text{eq}}$ ) and low-density vapor ( $\sim 0.2 \text{ g}\cdot\text{cm}^{-3}$ ) inclusions, coevally trapped at temperatures of 560–350 °C and pressures of 550–140 bar. Brine and vapor fluid inclusions are abundant within the deposit, extending down to depth of ~500 m below the ore body (Redmond et al., 2004). Sulfide precipitation in fractures was associated with retrograde quartz solubility upon cooling and vapor contraction

(Landtwing et al., 2010) and was introduced together with a second generation of quartz that preserves coeval brine (36–46 wt. % NaCl<sub>eq</sub>) and vapor inclusions trapped at 380–330 °C. Molybdenum mineralization occurred distinctly after copper mineralization (Redmond and Einaudi, 2010) and is proposed to be introduced by fluids of similar composition and evolution path, but precipitated at slightly different pH and redox conditions (Seo et al., 2012).

Globally, skarns are a typical feature of many porphyry systems (Sillitoe, 2010). Where porphyries intrude into carbonate-bearing sedimentary rocks, skarn mineralization develops. Proximal replacement skarns with coarsely crystalline calc-silicate Fe-Mg-Mn-rich mineral assemblages are formed by percolation and reaction of magma-derived fluids with the chemically reactive carbonate rocks. The association of skarns proximal to porphyry-copper deposits has been described from southwestern North America (e.g. Bingham Canyon, Copper Canyon, Ely, Twin Buttes, Yerington, and other districts summarized by Einaudi, 1982) and worldwide, e.g. Ok Tedi (Indonesia; van Dongen et al., 2010; Pollard, 2014) Grasberg (PNG; Graham et al., 2004), and Morococha (Peru; Catchpole et al., 2015).

Skarn-forming fluids generally share characteristics with the hosting porphyry intrusions in terms of fluid types, their salinities and homogenization temperatures (see summary in Meinert et al., 2005; and Bodnar et al., 2014). Skarn fluids show evidence for phase separation, high salinities and temperatures of formation that decrease with distance from the source and from early stage to late retrograde stage (e.g. Kwak, 1986; Meinert et al., 2003), and they have variably high CaCl<sub>2</sub> content (Kwak and Tan, 1981; Haynes and Kesler, 1988) and low CO<sub>2</sub> concentrations (e.g. Baker and Lang, 2003). Most fluid inclusion results come from transparent host minerals that are stable over broad *PT* ranges, such as quartz, carbonates or fluorite. The chemical composition of fluid inclusions hosted in such minerals have been studied by PIXE (Baker et al., 2003: proximal Cu skarn, Bismark, Mexico) and LA-ICP-MS microanalysis (Bertelli et al., 2009: Bismark, Mexico). The trace element composition of fluid inclusions hosted by calc-silicate skarn minerals remains largely unknown, except for the LA-ICP-MS study from a distal Pb-Zn-Ag skarn at the El Mochito deposit in Honduras (Ault, 2004; Samson et al., 2008), the Copper Canyon deposit at Battle Mountain (Nevada; Large et al., 2016) and a study of garnet-hosted inclusions from the Hongniu-Hongshan porphyry Cu-skarn system in China (Peng et al., 2015).

In the Bingham mining district, previous studies of skarns with regard to stratigraphy, mineralogy, structural geology, and chemical evolution have focused on the Carr Fork area that hosts high-grade gold and polymetallic mineralization in the contact aureole of the Bingham porphyry deposit (Hunt, 1924; Lindgren, 1924; Winchell, 1924; Hansen, 1961; Atkinson and Einaudi, 1978; Reid, 1978; Starkins, 1983; Cameron and Garmoe, 1987). The Carr Fork production shaft is located 5 km west of the center of the Kennecott Utah Copper Corp. (KUCC) open pit mine and the Carr Fork Canyon mine has been consumed by the current KUCC pit (Cameron and Garmoe, 1987). In 1896–1947 and 1979–1981, the Carr Fork mines (Utah Metal & Tunnel, Utah Consolidated, Highland Boy, Yampa,

Parnell, Utah Apex and other smaller mines) produced over 70 Mt of ore, i.e. over 70 % of the non-porphyry sulfide Pb, Zn, Cu, Ag, and Au ores of the Bingham district (Boutwell, 1905; Hansen, 1961; Cameron and Garmoe, 1987; Atkinson and Einaudi, 1978).

Fluid inclusions from the Carr Fork skarns were studied by Starkins (1983), focusing on variation in fluid types with horizontal distance from the intrusive contact and correlation of the fluid types with skarn formation stages. Starkins (1983) associates the early skarn alteration stage with existence of high salinity ( $> 60$  wt. %  $\text{NaCl}_{\text{eq}}$ ) and high temperature ( $> 600$  °C) fluid inclusions. Beginning of the main stage skarn alteration is typified by vapor-like  $\text{CO}_2$ -bearing fluid with salinity of 3–10 wt. %  $\text{NaCl}_{\text{eq}}$ , temperatures of trapping decreasing from 510 °C at the intrusion to 370 °C at the distance of 500 m from the contact. Boiling of hydrothermal fluids indicated by vapor and brine inclusions were related to the beginning of a hydrostatic regime. With progressive boiling, the vapor inclusions are described to change their salinity from 4 to less than 1 wt. %  $\text{NaCl}_{\text{eq}}$ , and to concentrate more  $\text{CO}_2$  (up to 3 mol. %), while the salinity in brine increase from 18 up to 45 wt. %  $\text{NaCl}_{\text{eq}}$ . This is consistent with decompression, late stage retrograde skarn formation, Au-Ag-Pb-Zn mineralization and late quartz-calcite veining with minor pyrite (Starkins, 1983).

The present study focuses on chemical composition of fluids responsible for the formation of prograde skarn occurring as dismembered bodies within the main porphyry stock at the Bingham Canyon Cu-Mo-Au deposit. Our aim is to use this intimate spatial relationship of the two ore types, to compare the evolution of fluids of likely similar origin but different reaction pathways due to the contrasting wall rock composition. These skarns are exposed in the KUCC open pit mine, in underground workings, and in drill core from deeper portions of the deposit. We present petrography and mineral chemistry of the skarn minerals, microthermometry and LA-ICP-MS data for fluid inclusions hosted in several associated minerals – garnet, pyroxene, and quartz. Obtaining reliable information about fluid composition in the complex calc-silicate host minerals is far from trivial, therefore the analytical and data treatment strategies had to be modified from conventional routines. We particularly wish to compare the chemical composition of fluid inclusions preserved in co-existing calc-silicate minerals in various parts of the deposit. Comparison of fluids entrapped in different minerals allow assessing phenomena of post-entrapment modification of fluid inclusions – as cation exchange between the inclusion and the surrounding environment is known to selectively affect quartz-hosted fluid inclusions (Li et al., 2009; Zajacz et al., 2009; Lerchbaumer and Audétat, 2012; Seo and Heinrich, 2013; Spencer et al., 2015; Rottier et al., 2017; Schläglova et al., 2017b). Fluid data from skarn minerals may further clarify the fluid evolution of the porphyry-skarn ore system as a whole.

## Geological Setting

### *Regional and local geology*

The Bingham deposit lies in the central part of the Oquirrh Mountains, near the eastern margin of the Basin and Range province, and on the Uinta Arch – an east-west-trending extensional structure that facilitated emplacement of Tertiary granitoid intrusions and coeval volcanic rocks (Butler et al., 1920; Welsh and James, 1961; Tooker, 1971; Vogel et al., 1997). The deposit comprises six major intrusive phases of late Eocene age, referred to as Bingham Stock (Butler et al., 1920), emplaced into anticline of a folded sedimentary rock sequence – the Oquirrh Group – with marine shelf facies of Upper Pennsylvanian age (Welsh and James, 1961); Fig. 1.

The Oquirrh Group is a thick sequence of sandstones, calcareous carbonaceous siltstones and cherty limestones (Boutwell, 1905). The upper two kilometers of the Oquirrh Group – the Bingham Mine Formation – consist predominantly of quartz sandstones (approx. 83 % of the formation; Atkinson and Einaudi, 1978). They are light tan, thin to medium bedded, often cross-laminated, very fine-grained and contain a silt and sand fraction with about 60 % quartz, microcline, sodic plagioclase, and calcite (Atkinson, 1975; Atkinson and Einaudi, 1978). The sandstones are interbedded with over 30 mappable units of limestones (Welsh and James, 1961) of which three major units bear the bulk of the economic mineralization studied here (Fig. 2): (1) the Jordan Limestone, up to 70 m thick unit at the base of the Bingham Mine formation, can be correlated to the Highland Boy Limestone at Carr Fork (Atkinson and Einaudi, 1978; Cameron and Garmoe, 1987); (2) the Commercial Limestone (or Yampa Limestone at Carr Fork) is up to 40 m thick and lies stratigraphically above an interlayer of the Middle Quartzite; (3) the Parnell Limestone, located in the upper parts of the formation, is up to 5 m thick unit, more sandy in composition and swells and pinches into calcareous sandstones (Hansen, 1961). Siltstones comprise 5–10 % of the Bingham Mine Formation and represent 20 cm to several meters thick transitional facies, grading laterally into sandstones or limestones (Atkinson and Einaudi, 1978).

Unaltered Jordan and Commercial Limestone units outside of the mine (e.g. in Middle Canyon) are black, thin- to medium-bedded fined-grained rocks ranging from sandy, silty or argillaceous, to nearly pure limestones. They contain chert nodules or bands (Boutwell, 1905; Welsh and James, 1961), and up to 1 wt. % organic carbon (Atkinson and Einaudi, 1978). Quartz and silicates vary from 10 to 65 % of the rock volume (Reid, 1978). The quartz-rich domains are generally silty, while the quartz-poor limestones (< 15 %) are typically more fine-grained (Atkinson and Einaudi, 1978). The matrix of the limestone contains fine-grained bioclastic calcite cemented by crystalline calcite and up to 4 wt. % dolomite (Atkinson and Einaudi, 1978; Reid, 1978). Commercial and Jordan Limestone units within 1500 m of the contact to the Bingham Stock were recrystallized to dark grey to white marble, with calcite grains of 50 µm in size (Boutwell, 1905; Reid, 1978).

The sedimentary units show evidence of multiple stages of deformation, the most prominent structures being associated with the Cretaceous Sevier orogeny (James et al., 1961b). Intensive

1  
2  
3  
4 faulting of the sedimentary units focused in the axial plane of folds indicates that this deformation  
5 happened prior to the thermal input from the intrusive units. The prominent Rood Fold, present in the  
6 northern portion of the district, has west-dipping axial plane, 45° plunge, and gently dipping northern  
7 limbs (20–35°) with more steeply dipping southern limb (15–50°) hosting the Pb-Zn replacement ores  
8 of Carr Fork (Kloppenburg et al., 2010). Bedding plane faults active during folding resulted in abrupt  
9 changes in lithologies (Hunt, 1924). Earlier Sevier stage thrusts and later extensional faults of the  
10 Basin and Range both influenced the location of intrusions and hydrothermal mineralization (James et  
11 al., 1961b; Tooker, 1971; Atkinson and Einaudi, 1978; Lanier et al., 1978; Kloppenburg et al., 2010).  
12  
13

14 The emplacement of the Bingham Stock into the Bingham Mine Formation was controlled by  
15 Eocene reactivation of northwest- and northeast-trending strike-slip faults (Kloppenburg et al., 2010).  
16 Intrusive dikes have northeast strike, thickening into northwest-trending apophyses. The 38 Ma-old  
17 (Parry et al., 2001) pre-mineralization equigranular monzonite (EM) was intruded by series of  
18 mineralization-related porphyry dikes (Redmond and Einaudi, 2010) within less than 0.32 Ma (von  
19 Quadt et al., 2011). These are, from the oldest to youngest: (1) quartz-monzonite porphyry (QMP), a  
20 350-m wide and approx. 2-km long dike-like body running through the center of the deposit (Porter et  
21 al., 2012) that consists of 50–60 vol. % phenocrysts of plagioclase, orthoclase, amphibole, biotite and  
22 rare quartz in an aplitic quartz-feldspar matrix (Redmond and Einaudi, 2010); (2) the latite porphyry  
23 (LP) northeast-striking dikes similar in composition to the QMP; (3) the biotite porphyry (BP),  
24 forming 2.5–4 m wide dikes, containing a higher amount of biotite phenocrysts and groundmass  
25 giving the unit darker color, which are locally Cu-mineralized; and (4) the quartz-latite porphyry  
26 breccia (QLPbx) and (5) the quartz-latite porphyry (QLP) occurring as up to 10-m wide dikes similar  
27 to QMP in composition but with lower amount of phenocrysts (only 30–40 vol. %) and prominent,  
28 resorbed quartz. This youngest intrusive unit is almost barren of copper and gold, but cut by  
29 molybdenite mineralization in late quartz veins.  
30  
31

#### 32 *Hydrothermal alteration and mineralization*

  
33

34 Most copper and gold mineralization and associated potassic alteration are related to intrusion of  
35 the QMP, the largest of the porphyry intrusions. In magmatic lithologies, three main alteration zones  
36 are recognized: (1) potassic alteration, centered around the QMP and hosting the copper ore body  
37 extending to EM; (2) propylitic alteration surrounding the ore body in EM only; and (3) a phyllitic  
38 alteration overprint of all intrusions and former alteration types (Landtwing et al., 2002; Redmond and  
39 Einaudi, 2010). Potassic alteration includes hydrothermal K-feldspar in the center and secondary Mg-  
40 rich biotite extending further out in early vein selvages (Lanier et al., 1978). Early propylitic alteration  
41 overprinted primary magmatic pyroxene, hornblende, and biotite by hydrothermal actinolite, chlorite,  
42 epidote and calcite. Later vein haloes and pervasive sericite with the addition of Fe ± Cu sulfide  
43 marks the late phyllitic alteration. During a late stage argillic alteration, plagioclase is mostly replaced  
44 by montmorillonite. In the zone of QMP and LP dikes, the alteration is pervasive, while outside of  
45 this zone, the alteration is structurally controlled.  
46  
47

1  
2  
3  
4 After every porphyry intrusion up to LP, the same sequence of veins was developed with  
5 diminishing intensity (Redmond and Einaudi, 2010; Gruen et al., 2010). From early to late, these are:  
6 (1) biotite veinlets, (2) early dark micaceous veins (EDM), and (3) A-type quartz stockwork veins.  
7 The A-type quartz veins are spatially related to most of the Cu-Au mineralization, but bornite and  
8 chalcopyrite invariably precipitate by late reactivation and re-dissolution of earlier vein quartz  
9 (Redmond et al., 2004; Landtwing et al., 2005; Landtwing et al., 2010). The main copper minerals are  
10 chalcopyrite, bornite and digenite. Gold and silver are found as inclusions in bornite, both spatially  
11 following the copper mineralization while the grades can be correlated (for details on metal grades,  
12 see e.g. Porter et al., 2012). Molybdenum mineralization in quartz-molybdenite veins cross-cuts even  
13 the latest dyke contacts (Redmond and Einaudi, 2010; Seo et al., 2012). Despite later timing, Mo  
14 grade distribution broadly follows the Cu ore shell, but displaced downward and inward (Gruen et al.,  
15 2010; Seo et al., 2012). Pyrite veins with sericite haloes and locally some chalcopyrite postdate all  
16 veins and igneous intrusions (Redmond and Einaudi, 2010).  
17  
18

19 Calc-silicate mineral assemblages were developed at the contact of intrusions with sediments of  
20 the Bingham Mine Formation: skarns at the expense of nearly pure to silty limestones, and diopside  
21 hornfels after silty and carbonaceous sandstones and siltstones (Fig. 3). Spatial alteration zoning  
22 depends on the composition of the protolith and the distance from the intrusive stock, affecting  
23 temperature and fluid composition (Atkinson, 1975; Atkinson and Einaudi, 1978; Reid, 1978).

24 *In relatively pure major limestone units*, when approaching the stock, the calc-silicate assemblages  
25 are: (1) white recrystallized marble containing calcite, quartz, and chert; (2) wollastonite skarn zone  
26 including pyroxene, calcite, and quartz; and (3) garnet skarn zone with minor pyroxene, quartz, and  
27 calcite, proximal to the stock. The boundaries between these skarn zones are gradual, with calcite in  
28 the matrix generally diminishing towards the stock (Reid, 1978). Intrusive contacts against skarn and  
29 hornfels are sharp (e.g. Fig. 4A), but alteration extends into the intrusive rocks as endoskarn (EN; Fig.  
30 4G), where igneous textures are overprinted by potassic alteration in addition to formation of calc-  
31 silicate minerals including actinolite, epidote, and chlorite.

32 *In calcareous sandstones and siltstones*, pervasive pyroxene alteration is typical (Figs. 4A-C). It  
33 extends up to 1200 m away from the intrusive contact and is strongest along faults and fractures  
34 (Atkinson, 1975). The resulting pyroxene hornfels is very fine-grained, with single diopside grains of  
35 only a few microns in size. It is pale to light green and weathers to a buff or white color (Fig. 4F).  
36 With increasing distance from the stock, the assemblage pyroxene-quartz-calcite is prevalent. Calcite  
37 has undergone Mg metasomatism (up to 4 mol. % Mg), extending beyond the pyroxene alteration  
38 zone.

39 Temporally, the skarns and hornfels record three stages of superimposed alteration (Atkinson and  
40 Einaudi (1978), so that not all mineral zones shown in Fig. 3 are preserved everywhere.

*Early stage contact metamorphism and alteration*, possibly associated with minor addition of magnesium and silica to the rocks, resulted in pervasive pyroxene formation in calcareous quartzites and siltstones (forming up to 35 % diopside in the rock), while purer limestones developed wollastonite with minor pyroxene, vesuvianite and sulfides (Atkinson and Einaudi, 1978). Approaching the stock, chert nodules in the limestone become bleached, develop a wollastonite rim, or are completely replaced by wollastonite. Bulk chemistry of the unaltered limestones from Middle Canyon in comparison to the skarns of the Bingham mine (lithologies from both the locations belong to the Commercial Limestone unit) show that the alteration was accompanied by strong addition of SiO<sub>2</sub>, Al<sub>2</sub>O<sub>3</sub>, MgO, MnO, TiO<sub>2</sub>, and BaO but depletion in CaO and CO<sub>2</sub> (Reid, 1978). The alteration extent is controlled by local structural complexities and lithology. This alteration appears to be absent in igneous rocks (Lanier et al., 1978).

The main skarn stage is considered contemporaneous with potassic alteration and quartz-sulfide veining in the porphyries, based on vein relationship at intrusive contacts (Atkinson and Einaudi, 1978). In limestones, wollastonite and pyroxene were replaced by garnet. Some wollastonite can be preserved in centers of thick limestone units and its occurrence becomes restricted with depth. In some places, garnet growth has completely obliterated wollastonite and garnet skarn is therefore in direct contact with recrystallized marble. Garnet has formed preferentially along fractures, as cm- to m-wide zones of selective replacement. Garnets show oscillatory zoning of grossular to andradite in composition, while texturally earlier pyroxenes are usually very fine-grained or recrystallized, ranging from diopside to salite – an intermediate composition of the diopside-hedenbergite series (Atkinson, 1975). Later in the main stage, garnet is partially destroyed and replaced by calcite and quartz, iron oxides, and sulfides including pyrite and chalcopyrite (Atkinson and Einaudi, 1978). Magnetite and less commonly hematite are present mostly in sulfide veins, associated with pyrite. In the hornfels derived from calcareous siltstones, the main skarn stage is characterized by bedding streaks and orbicules of actinolite and biotite and quartz-sulfide veinlets with actinolite selvages.

The late retrograde skarn stage is characterized by formation of hydrous minerals, such as epidote, actinolite, and chlorite, in addition to pyrite, along re-opened veins and as replacement of anhydrous assemblages (Atkinson and Einaudi, 1978). This stage is contemporaneous with formation of sericite and pyrite in the intrusive units. Late stage argillic alteration includes formation of chlorite, montmorillonite group clays (saponite, Fe-saponite, nontronite), hydromuscovite, talc, and pyrite in the hornfels and in lower abundance also in the skarns. Approaching the stock, actinolite is commonly replaced by biotite, and texturally changes from compositional bands into patches and fracture envelopes. In the deeper part of the deposit, late zeolite minerals, such as stilbite, are present (Stephens and Bray, 1973).

The copper mineralization in the altered sedimentary units is generally erratic but most prominent in the inner high-silica garnet-quartz endoskarn as part of the QMP copper ore shell. Principal ore minerals in the skarn are chalcopyrite, associated with pyrite and magnetite present as veins or

dissemination (Cameron and Garmoe, 1987). In the siliciclastic precursors, notably rather pure quartzites, nukundamite ( $\text{Cu}_{3.38}\text{Fe}_{0.62}\text{S}_4$ ) formed during the main potassic and skarn stage, partly replaced by later chalcopyrite and bornite (Inan and Einaudi, 2002). At Carr Fork skarn, there are two distinct gold mineralization stages – first during the porphyry copper mineralization and second as later enrichment occurring with high pyrite content and clay minerals (Cameron and Garmoe, 1987). The highest Au grades commonly occur in strongly silicified or pyrite-rich skarns. Gold occurs as fine particles,  $<25\ \mu\text{m}$  in size, hosted within or at the boundaries of the sulfides, mostly bornite and chalcopyrite (Ballantyne et al., 1997). Ore grades and alteration intensity extending beyond the regular ore shell are mainly controlled by fractures and faults in a system of northeast-striking structures (Atkinson and Einaudi, 1978). With increasing distance from the Stock, pyrite, galena and sphalerite predominate (Reid, 1978).

## Sampling and Methods

We selected several vertical NNW-SSE trending cross sections through the deposit to sample compact and weakly retrograded skarns from the Commercial and Jordan Limestones, and from an isolated skarn raft in the recently drilled deep hole D794 accessing the barren core of the deposit. Our samples include 97 drill core samples from the repository of Kennecott Utah Copper Corp. (KUCC) and 12 hand specimens of high-grade garnet skarn from the Commercial Limestone unit outcropping in the open pit (outcrop at: N  $40^{\circ}31'17.5$ , W  $112^{\circ}08'40.2$ , accessed June 2014). The principal section labeled N-1400 (Figs. 1, 2) runs through the center of the deposit, and a similar but inclined section has been previously studied for vein geometry by Gruen et al. (2010). Both are perpendicular to section E-1400 used for fluid inclusion studies by Landtwing et al. (2005; 2010). Information about sample location and their petrography, can be found in the electronic appendix.

Backscattered electron images and mineral identification have been performed using a JEOL JSM-6390 OLA scanning electron microscope (SEM) at ETH Zurich with 15 kV acceleration voltage, 32–45 nA beam current and  $\sim 70\ \text{nm}$  spot size. Major-element analyses have been obtained using calibrated silicate analysis, and recalculated based on Grew et al. (2013) and Morimoto et al. (1988) for garnets and pyroxenes, respectively. All mineral abbreviations follow Whitney and Evans (2010).

Cathodoluminescence (CL) of quartz was studied by an SEM-mounted Centaurus detector with the same operating conditions. The SEM-CL of the skarn samples proved to be challenging likely due to a high relief contrast between quartz and the interstitial calcite and due to a high porosity of the samples. The fractures and lower areas with softer minerals (e.g. calcite) induce a bright memory effect on the detector and thus prevent obtaining any good quality picture. Optical cold-cathodoluminescence (Luminoscope ELM-3R) at the University of Freiburg (Germany) was therefore tested. The samples were irradiated in a vacuum chamber mounted on an optical microscope, with an electron beam of 5–15 kV and a current of 0.5–1.5 mA under vacuum of 10–60 mTorr. Luminescence of quartz proved to be too weak but the method can recognize calcite in fine-grained veins that are difficult to see by optical microscopy of thick sections.

1  
2  
3  
4 Microthermometric measurements of fluid inclusions in quartz, garnet, and pyroxene were  
5 performed using a Linkam THSMG 600 heating-freezing stage, calibrated with Synflinc standards  
6 ( $T_m \text{ CO}_2 = -56.6 \pm 0.2 \text{ }^\circ\text{C}$ ,  $T_m \text{ ice} = 0 \pm 0.1 \text{ }^\circ\text{C}$ ,  $\text{Th H}_2\text{O} = 374.1 \pm 1.5 \text{ }^\circ\text{C}$ ). Total salinity of the fluid  
7 inclusions (wt. % NaCl equivalent) was calculated using the models of Sterner and Bodnar (1989),  
8 Bodnar (1993), and Lecumberri-Sanchez et al. (2012), incorporated in Steele-MacInnis et al. (2012).  
9 The low temperature observations and halite dissolution were measured prior to the LA-ICP-MS  
10 analyses. Homogenization temperatures above ca.  $370 \text{ }^\circ\text{C}$  were obtained afterwards on remaining  
11 inclusions, to avoid decrepitation and potential diffusion of cations between the inclusion and the host  
12 (see e.g. Rottier et al., 2017).

13  
14 The ETH-prototype ArF 193-nm Excimer laser system (Geolas, Lambda Physik, Germany)  
15 coupled to a fast-scanning sector-field ICP-MS (Element XR, Thermo Scientific, Germany) was used  
16 for all fluid inclusion analyses (Table 1). We used a laser pulse rate of 10 Hz for all analyses and a  
17 spot size of  $40 \mu\text{m}$  for reference materials. The sampling of fluid inclusions was done using an iris  
18 aperture for gradual opening from 0 up to  $120 \mu\text{m}$ , allowing complete ablation of the inclusion. We  
19 used laser output energies of ca. 80 to 120 mJ, corresponding to energy densities of ca.  $9\text{--}15 \text{ J}\cdot\text{cm}^{-2}$  on  
20 sample. Samples were rubbed in  $1\text{-}\mu\text{m}$  alpha-alumina suspension (Struers, Denmark), while the  $\sim 1$   
21  $\text{cm}^3$  all-glass sample chamber was additionally washed in aqua regia to minimize contamination. We  
22 used fluorinated ethylene propylene (FEP) tubing (Rotilabo®, Carl Roth GmbH, Germany) to connect  
23 the ablation cell to the ICP-MS, and skimmer and sampler cones made of Ni, cleaned with HF  
24 (Schlöglöva et al., 2017a). We used  $1.0\text{--}1.1 \text{ L}\cdot\text{min}^{-1}$  of 5.0 grade He as carrier gas merged with  $0.75\text{--}$   
25  $0.95 \text{ L}\cdot\text{min}^{-1}$  of 6.0 grade Ar sample gas downstream from the sample chamber. The ICP-MS was  
26 optimized for maximum sensitivity on high masses ( $^{232}\text{Th}$ ,  $^{238}\text{U}$ ) and low oxide formation ratio (<  
27  $0.3 \text{ \% ThO}^+/\text{Th}^+$ ). We used the following element menu:  $^7\text{Li}$ ,  $^{11}\text{B}$ ,  $^{23}\text{Na}$ ,  $^{24}\text{Mg}$ ,  $^{27}\text{Al}$ ,  $^{29}\text{Si}$ ,  $^{34}\text{S}$ ,  $^{35}\text{Cl}$ ,  $^{39}\text{K}$ ,  
28  $^{43}\text{Ca}$ ,  $^{55}\text{Mn}$ ,  $^{57}\text{Fe}$ ,  $^{65}\text{Cu}$ ,  $^{66}\text{Zn}$ ,  $^{75}\text{As}$ ,  $^{79}\text{Br}$ ,  $^{85}\text{Rb}$ ,  $^{88}\text{Sr}$ ,  $^{95}\text{Mo}$ ,  $^{107}\text{Ag}$ ,  $^{118}\text{Ag}$ ,  $^{118}\text{Sn}$ ,  $^{121}\text{Sb}$ ,  $^{133}\text{Cs}$ ,  $^{137}\text{Ba}$ ,  $^{181}\text{Ta}$ ,  
29  $^{182}\text{W}$ ,  $^{197}\text{Au}$ ,  $^{208}\text{Pb}$ ,  $^{209}\text{Bi}$ ,  $^{238}\text{U}$ . Dwell times for all elements were set to 20 ms, with exception of Na,  
30 K, S, Pb (50 ms), Cl, Br (100 ms), and Au (200 ms).

31  
32 The LA-ICP-MS signals were treated with the Matlab-based program SILLS (Guillong et al.,  
33 2008) with limits of detection calculated following Pettke et al. (2012). The fluid inclusion data have  
34 been revised for falsely positive numerical values, i.e. only signals that have clearly visible fluid  
35 inclusion peak rising statistically above host background are considered significant. All analyses were  
36 calibrated against the external standard NIST SRM 610. The concentrations in the host minerals were  
37 determined using their average  $\text{SiO}_2$  content (100 wt. % for quartz, 36 wt. % for garnet, and 53 wt. %  
38 for pyroxene) based on EDX analyses (see Tables 2-3) as internal standard. Absolute concentrations  
39 of the trace elements in fluid inclusions were obtained by referencing element ratios against  
40 microthermometrically determined salinity. Where possible, we used the salinity (wt. %  $\text{NaCl}_{\text{eq}}$ ) of  
41 the respective fluid inclusions, or the average value for a fluid inclusion assemblage.

The microthermometry and element ratios from LA-ICP-MS analyses revealed that besides NaCl, the inclusions contain non-negligible amounts of K, and potentially Ca and Fe as chloride compounds. In garnet and pyroxene, Ca and Fe in fluid inclusions cannot be analyzed by LA-ICP-MS due to their presence as major elements in these host minerals, and limited visibility in these minerals also prevented accurate determination of the hydrohalite melting temperatures (Schlegel et al., 2012). The absolute trace element concentrations in the fluid inclusions reported here were therefore calculated using NaCl wt.% equivalent salinity as internal standard, and corrected only for the presence of K (the ratio to Na being based on relative intensities from the LA-ICP-MS signal; Heinrich et al., 2003). Given these uncertainties on the absolute trace element concentrations in fluid inclusions, the discussion and comparison to other fluid inclusions studies from Bingham are based on elemental ratios to Na, which are independent of any internal standard.

## Skarn Mineral Paragenesis

Evaluation of mineral assemblages is based upon petrographic relations visible on polished rock slabs and in thin sections studied by transmitted and reflected light microscopy and SEM (BSE imaging and EDX analyses). Our main focus was on representative skarn samples from the Commercial, Jordan, and deep Limestones. For petrography and veining relations, samples of hornfels in the same sections and drill holes were also compared, showing a broadly similar paragenetic sequence. Fig. 5 shows photomicrographs, which together with the macroscopic relations on Fig. 4 and data from the published literature lead to the paragenetic summary diagram shown in Fig. 3.

*Pyroxene* is the earliest mineral phase preserved in the skarns. It first occurs as early contact-metamorphic rounded diopside grains (*PX1*; Di<sub>98</sub>Hd<sub>02</sub> – Di<sub>76</sub>Hd<sub>24</sub>; Table 2), few microns in size, locally recrystallized. Early contact-metamorphic diopside is pale to white (Figs. 4C-E, H) or light green in color (Figs. 4A-B) and appears as nearly euhedral inclusions in garnet and also as rounded grains in some sulfides (Fig. 5A). It is preserved together with minor wollastonite relics. The recrystallized diopside grains (*PX2*, Fig. 4E) are up to 2 mm large, have interlocking or decussate textures and are locally enriched in iron, ranging from Di<sub>94</sub>Hd<sub>06</sub> to Di<sub>50</sub>Hd<sub>50</sub> (“salite”). They can form along fractures or in patches, preserving numerous fluid inclusions in the intact cores. The pyroxene from the deep skarn unit is generally coarser grained, partially altered to ferroan diopside (Di<sub>94</sub>Hd<sub>06</sub> – Di<sub>58</sub>Hd<sub>42</sub>), but noticeably better preserved and more abundant, when compared to the Commercial and Jordan Limestone units in the center of the deposit. In the center of the deposit, pyroxene is commonly replaced by retrograde stage amphibole (actinolite), calcite and locally hematite (Figs. 4A-D, 5B). In the hornfels, pyroxene is the main rock-forming mineral, preserved in pale to almost white variety or as light green homogeneous fine-grained diopside mass without usable fluid inclusions.

*Garnet* forms occasional disseminations in the pyroxene groundmass of the skarns or is present as massive replacement zones along fractures or following primary bedding, as indicated by local folds (Figs. 4C, H). Garnet occurs as fine- to coarse-grained aggregates of anhedral to euhedral grains of yellow-brown to dark red in color (Figs. 4C, H). They show complex growth and several generations

of variable composition (Table 3). Cores of the garnet aggregates commonly contain abundant inclusions of early diopside imparting a sieve or atoll texture, with cores commonly resorbed and replaced by hydrous minerals and/or quartz, calcite and sulfides, or a new generation of garnet. We identified three major garnet generations: (1) the earliest but rarely preserved light red to pink grossular cores (*GRT1*;  $\text{Adr}_{23}\text{Grs}_{77}$  –  $\text{Adr}_{47}\text{Grs}_{53}$ ; Fig. 5C); (2) dark red Al-poor or Al-free andraditic garnet (*GRT2*, from  $\text{Adr}_{85}\text{Grs}_{15}$  up to  $\text{Adr}_{100}\text{Grs}_{00}$ ; Fig. 5D), often optically anisotropic and with up to 0.5 OH apfu; (3) and orange-red Al-rich andradite (*GRT3*;  $\text{Adr}_{74}\text{Grs}_{26}$  –  $\text{Adr}_{86}\text{Grs}_{14}$ ; Fig. 5E) replacing cores of the older generations (Fig. 5D), cross-cutting in form of irregular veins and patches or overgrowing them (Fig. 5E). Variation of the garnet chemistry might be attributed to local heterogeneities in the protolith or changing fluid chemistry and redox conditions. All studied fluid inclusions are hosted in the growth zones of the Al-poor andraditic garnet (*GRT2*) and in the latest Al-rich andradite generation (*GRT3*).

*Quartz-calcite veins*, patches and embayments flood the relics of pyroxene matrix in skarns (Fig. 5A), with fractures and fissures in garnet showing late introduction of this assemblage (Fig. 5E). The garnet grains suffer partial destruction from their edges and are typically fragmented and re-cemented by quartz and calcite. Quartz forms patches of rounded or euhedral grains with only weak luminescence and zoning with darker cores and brighter rimes. Calcite typically grows either along the quartz grains and vein edges (Fig. 5F), forms interstitial mass between the quartz grains or cuts across the quartz as separate veins. Based on this relationship, calcite postdates the formation of quartz. Calcite replaces diopside in the matrix and some of the pyroxene inclusions in garnet. The quartz-calcite veins are often complex in geometry and also mineralogy – some containing pyrite and chalcopyrite in the central parts in the quartz mass and magnetite and pyrite at their edges, while others have chalcopyrite and pyrite in the calcite groundmass.

*Sulfides* form either massive patches or disseminations in the quartz-calcite mass (Figs. 4D, F) or can be present as sulfide-dominated fracture fills in garnet (Figs. 4H, 5I) but do not occur as obvious inclusions overgrown by garnet. In the hornfels, sulfide mineralization is typically seated in quartz-calcite veinlets with actinolite haloes. The most abundant sulfide mineral is pyrite, often accompanied by magnetite. Early pyrite forms veins and clusters enclosing grains of pyroxene (Fig. 5A), and rarely also quartz and garnet. Pyrite can be also found as inclusions within garnet, rarely along growth zones or garnet cores. This indicates some early pyrite formation but in most cases, the pyrite and also chalcopyrite penetrate along microfractures and infill the atoll garnet cores later (Fig. 5H). Pyrite grains have often resorbed edges or are fractured and filled by calcite and some quartz, indicating that some of the pyrite was formed prior to or during the major input of quartz and calcite into the rock. Chalcopyrite and some minor bornite follow the formation of pyrite, growing on its edges (Fig. 5J). Apparent inclusions in pyrite are related to microfractures, therefore chalcopyrite is interpreted to be a later phase. In the quartz-calcite veins, pyrite and chalcopyrite occur as disseminated grains in the center of the quartz veins or in the interstitial mass of calcite (Figs. 4F, 5F). Most sulfide precipitated after the formation of quartz and prior or contemporaneously with the calcite. In garnet, the evidence

is ambiguous – sulfide-only veins form either directly after the latest garnet generation (*GRT3*) or replace interstitial calcite and thus postdate the garnet (*GRT3*, e.g. Figs. 5E, I). Molybdenite was found in late quartz-dominated veins, crosscutting previous sulfide stages in the skarns/hornfels (Fig. 4B).

*Iron oxides* associated with skarn alteration are magnetite and hematite. Magnetite is more abundant in the deeper portions of the deposit. In the top parts, lower amounts of magnetite coexists locally with specular hematite or forming martite with fibrous texture. The magnetite in the upper parts of the deposit is most commonly associated with sulfide-rich zones.

*Hydrous minerals* are related to the retrograde stage of skarn formation (Fig. 4D). Amphibole commonly replaces pyroxene along fractures and quartz-calcite veins in both skarns and hornfels, progressing into the pyroxene matrix (Figs. 4A-B). Pyroxene grains are replaced from their grain edges by brown fibrous actinolite (Fig. 5B). Epidote forms grains and patches interstitial to garnet, pyroxene, and amphiboles (Fig. 4D), containing commonly rounded sulfide grains. Minor biotite may replace garnet and pyroxene, commonly within and close to the endoskarn (Fig. 4G). Chlorite fills parts of the quartz-calcite veins in fractured garnet and is commonly associated with amphibole and biotite replacement. The latest minerals are clays, filling pockets in porous garnet-rich areas. Minor fibrous zeolite (likely stilbite) was observed in centers of the quartz-calcite veins in the skarn and monzonite from the deep barren core.

*Accessory minerals* in the skarns are apatite, present typically in garnet, and zircon in pyroxene and amphibole. Minor vesuvianite associated with pale diopside and early garnet can be found. In retrograde samples, anorthite, interstitial to garnet and amphibole can be found. By LA-ICP-MS analyses of the fluid inclusion hosting minerals, we documented presence of submicroscopic inclusions of galena, sphalerite, chalcopyrite, and wolframite/scheelite (only W peaks recorded) in amphibole, molybdenite and likely scheelite in garnet and pyroxene, and electrum and anhydrite in the fine-grained quartz-calcite veins.

## Fluid inclusion petrography and microthermometry

### Classification

Fluid inclusions were observed in large recrystallized pyroxene grains (*PX2*), andraditic garnet (*GRT2* and *GRT3*), and quartz of the main skarn alteration stage and in amphibole and epidote from the retrograde stage. Rarely, fluid inclusions were also preserved in coarse grained calcite from the quartz-calcite veins in the deep barren core. All fluid inclusions were classified based on their relation to the host crystal following the criteria of Roedder (1984). Majority of fluid inclusions presented in this study do not appear in well-defined linear trails – they form clusters and densely populated fluid inclusion assemblages. In case of garnet, the concept of fluid inclusion assemblage was relaxed from a single mineral grain to multiple neighboring mineral grains hosting inclusions with optically identical phase proportions.

Inclusions in visible garnet growth zones (*GRT2*, Fig. 6D) or in the alteration patches of the latest garnet generation (*GRT3*, Figs. 6E-F) are clearly primary. Inclusions hosted in quartz (Figs. 6G-H), forming clusters in centers of the dark luminescent grains, are probably pseudosecondary. The Fe-rich patches in diopsidic pyroxene (*PX2*) observed during BSE imaging and EDX analysis, host inclusions (Figs. 6A-B) that are probably related to the main stage skarn alteration, obliterating any earlier inclusions that might have formed during the contact metamorphism and Mg-rich diopside growth (*PXI*). Rare calcite-hosted inclusions are likely of secondary origin, cutting the mineral cleavage (Fig. 6I). Amphibole and epidote host inclusions that are likely of primary origin, aligned with fibrous texture of amphibole and in centers of epidote crystals. However, they show inconsistent phase proportions within inclusion assemblages and are rich in salts and solid phases; they were therefore not considered further.

Four types of fluid inclusions based on their content and appearance at room temperature were distinguished: aqueous (AQ), intermediate-density (ID), vapor-dominated (V), and brine (B). Aqueous inclusions (AQ) contain more than 60 % of liquid. They can be found as pseudosecondary or secondary trails in the andraditic garnet (*GRT2*, Fig. 6C) and as secondary inclusions in calcite (Fig. 6I). Intermediate-density inclusions (ID) with ~40–70 % vapor bubble are typical for the deep barren core of the deposit and are also present in the andraditic garnet growth zones (*GRT2*, Fig. 6D), in the center of pyroxene grains (*PX2*, Fig. 6A), and in quartz grains (Fig. 6H). Occasionally, ID inclusions are also found in the upper parts of the deposit, most commonly in pyroxene. ID inclusions in quartz from the deep barren core are rarely well preserved, mostly having irregular shape and showing signs of sweat-halo and shearing. Vapor inclusions with over 70 % of vapor bubble (type V), and brine inclusions (type B), containing one or two salt crystals (halite ± sylvite) at room temperature (Fig. 6G), are the main types of inclusions present in quartz formed during the main stage skarn alteration. Both also occur in the Al-rich andradite patches of the latest garnet generation (*GRT3*; Figs. 6E-F) and less commonly also in recrystallized pyroxene grains (*PX2*; Fig. 6B). The garnet commonly preserves single, isolated, large inclusions of irregular shape and with similar phase proportions between several garnet grains in a sample, but rarely distinct trails or primary growth arrays (e.g. sample BC14-P01). Many of the inclusions – especially brine and vapor types – contain daughter crystals, such as one or two opaque phases (hematite or/and chalcopyrite or pyrite, based on color and shape of the phases) and a birefringent mineral that does not dissolve upon heating (likely calcite or anhydrite). The size of the daughter phases is not always proportional to the size of the inclusions, indicating accidental trapping, most commonly of hematite in garnet-hosted inclusions. Pyroxene occasionally preserves brine inclusions that are very rich in solid phases – salts or other transparent minerals – and commonly have a very small vapor bubble (20 % or less, some none at all). They might contain excess salt by loss of water to amphibole formed by internal reaction.

Size and shape of fluid inclusions vary greatly. Garnet preserves very small (1–20 µm) primary inclusions along growth zones in the Al-poor andraditic variety (*GRT2*), whereas Al-rich andradite patches (*GRT3*) contain inclusions up to 500 µm in size. The morphology of the latter is commonly

very complex, with internal steps and facets determined by host crystallography, suggesting a primary origin for these inclusions. Pyroxene and quartz both host elongated, round or negative crystal-shape inclusions ranging from 5 to 40  $\mu\text{m}$  in size. For summary of fluid inclusion types and physico-chemical characteristics, see Table 4.

#### Microthermometry

We conducted microthermometric measurements on over 250 fluid inclusions in 10 samples from various locations within the deposit. The salinities of vapor, brine and intermediate-density inclusions in quartz, garnet and pyroxene are all in the same ranges for the respective fluid types, alike the homogenization temperatures (see Fig. 7 and Table 4). The complete set of the microthermometry results can be found in the electronic appendix.

To estimate their salinity, aqueous, intermediate-density, and vapor inclusions were cooled below -150 °C and then slowly heated, commonly using the temperature cycling method (Haynes, 1985; Zwart and Touret, 1994; Schlegel et al., 2012). Upon warming, the brownish homogeneous ice texture clears between -68 and -49 °C, indicating a low eutectic due to the presence of salts other than NaCl and KCl, such as CaCl<sub>2</sub> or FeCl<sub>2</sub> (Steele-MacInnis et al., 2016). No clathrate formation and melting was observed at higher temperature, arguing against the presence of significant CO<sub>2</sub>. In intermediate-density inclusions in quartz, melting of light greenish hydrohalite was recorded between -27 to -21 °C. In vapor inclusions, melting of hydrohalite was observed only rarely, at -23 to -21 °C. The last phase to melt was ice, at temperatures of -17.5 to -6 °C in the intermediate-density inclusions and -6.8 to -1.2 °C in the vapor inclusions. The ice melting temperatures in the ID inclusions return 7–20 wt. % NaCl<sub>eq</sub>, averaging at 15 wt. % NaCl<sub>eq</sub>. Vapor inclusions hosted in garnet and quartz, yield salinity of 1.8–7.2 wt. % NaCl<sub>eq</sub>. Pyroxene-hosted vapor inclusions are very small and difficult to observe due to the darkness of the host mineral, therefore changes upon freezing and heating were observed only rarely. The aqueous inclusions hosted in garnet (*GRT2*) and calcite have not been systematically studied – the garnet-hosted inclusions yielding very heterogeneous ice melting temperatures (from -2 to over -20 °C) within an assemblage, while the calcite-hosted inclusions are very small in size. Additionally, the double refraction of calcite impaired the visibility.

Salinity of brine inclusions was determined upon heating. Brines with visible sylvite crystal, preserved in quartz, show dissolution of sylvite around 125 °C. The halite then dissolves between 255 and 395 °C. Quartz-hosted brine inclusions have salinity of 37–42 wt. % NaCl<sub>eq</sub>. Brine inclusions in garnet and pyroxene have typically only one visible salt crystal dissolving at 220–305 °C and 270–370 °C, respectively, yielding salinities of 32–38 and 36–42 wt. % NaCl<sub>eq</sub>.

The ID inclusions with density of ~0.6–0.7 g·cm<sup>-3</sup> homogenize near-critically – by meniscus fading or to the liquid – at temperatures of 355–395 °C in all minerals and locations. Homogenization temperature of the vapor inclusions in quartz and garnet ranges from 385 to 442 °C. Most brine inclusions homogenize to liquid at Th = 345–428 °C and only a small number of sylvite-bearing

1  
2  
3  
4 brines homogenize by halite disappearance. The salt- or solid phase-rich pyroxene-hosted inclusions  
5 fail to show any changes when heating up to 450 °C.  
6  
7

## 8 Fluid chemistry 9

10 Elemental composition of 520 single fluid inclusions preserved in various skarn minerals have  
11 been obtained by LA-ICP-MS analysis, using eight carefully selected samples from three locations  
12 within the deposit: (1) The Au-Cu center of the deposit, located at the very top and sampled in the  
13 open pit, hosting brine and vapor inclusions from coeval garnet and quartz; (2) The Cu-rich periphery,  
14 where availability of well-preserved brine and vapor inclusions in all, coeval host minerals (garnet,  
15 pyroxene and quartz) is the best; (3) the deep barren core, hosting only the intermediate-density  
16 inclusions in all three host minerals (garnet, pyroxene and quartz).  
17  
18

19 The number of quantifiable elements in fluid inclusions hosted by complex calc-silicate minerals is  
20 limited. Garnet and pyroxene both contain Mg, Ca, Mn, and Fe up to tens of wt. % so that these  
21 cations cannot be analyzed in the fluid inclusions (Figs. 8A-B). Moreover, garnet and pyroxene  
22 contain variable quantities of many trace elements (Figs. 8C-D). Garnet contains approx. 0.1–0.5 ppm  
23 B, 1–10 ppm Na, 2–5 ppm Zn, 5–10 ppm As, 0.5–2 ppm Mo, 50–300 ppm W, 0.1–0.5 pm Pb, 0.02–  
24 0.05 ppm Bi, and 1–15 ppm U (Fig. 9). Pyroxene trace element composition is in the range of 0.5–1  
25 ppm Li, 1–5 ppm B, 100–500 ppm Na, 5–20 ppm K, 100–300 ppm Zn, 0.1–0.3 ppm As, 10–50 ppm  
26 Sr, 0.05–0.2 ppm Ag, 0.1–0.5 ppm Ba, 0.01–0.08 ppm W, and 0.5–2 ppm Pb (Fig. 9). The high  
27 concentrations of As, Mo, and W in garnet, and Zn in pyroxene prevented recording of a fluid  
28 inclusion peak for these elements. Only rare but high signals (up to units of wt. % in concentration)  
29 for Mo and W in garnet-hosted inclusions were found, likely indicating an accidental entrapment of  
30 respectively molybdenite and an W-bearing phase, e.g. wolframite or scheelite. The vapor and brine  
31 inclusions hosted in garnet are typically found in the Al-rich andradite patches (*GRT3*, Figs. 6E-F,  
32 8C) that coincide with zoning and elevation in Na, Mo and Sn but decrease in Fe, As, and W.  
33  
34

35 We have not been able to record any Sn signal in the fluid inclusions. In addition to elevated  
36 content of Sn in the host minerals including quartz, we suspect some Sn contamination in the LA-ICP-  
37 MS system, adding to the host signal (Schlögl et al., 2017a). Garnet can contain up to 0.3 ppm Ta  
38 and its oxide ( $^{181}\text{Ta}^{16}\text{O}$ ) interferes on the mass of  $^{197}\text{Au}$ . However, no tantalum was recorded in the  
39 fluid inclusions, as the instrument was optimized for low oxide formation rate (< 0.25 %); therefore,  
40 any interference on the Au isotope can be ruled out. Gold was detected in approximately 65 % of the  
41 inclusions, visible as prominent peak correlated with the main elements in the fluid inclusion (Na, K,  
42 Cl, Pb; Fig. 8A). Owing to the elevated instrumental background (Figs. 8A-B), sulfur was recorded  
43 only in the largest inclusions (< 10% of inclusions). Positive sulfur analysis may coincide with  
44 presence of chalcopyrite or other sulfide crystals inside the respective fluid inclusion.  
45  
46

47 Due to the uncertainties regarding absolute concentrations, described in the Methods section, we  
48 compare the fluid composition from the different host minerals as cation ratios relative to Na –an  
49

1  
2  
3  
4 element recorded in all fluid inclusions above ca. 10  $\mu\text{m}$  in size and our best proxy for the fluid  
5 salinity. Sodium can be present as trace element in the pyroxene (up to 20 ppm) and garnet (up to 10  
6 ppm). However, in pyroxene, the Na content may vary throughout the ablation of a single spot (Figs.  
7 8B, D) so that the correction from Na contribution of the host might not be fully accurate, thereby  
8 propagating an uncertainty into the elemental ratios and concentration results. Furthermore, most of  
9 the pyroxene-hosted fluid inclusions are small (10–25  $\mu\text{m}$ ) and thus have low Na signal, adding to the  
10 uncertainty of the analyses. The pyroxene data must be therefore regarded with caution. For LA-ICP-  
11 MS results from all the analyzed single fluid inclusions, the reader is referred to the electronic  
12 appendix.  
13

14 Samples from the Au-Cu center and the Cu-rich periphery (Figs. 10A-B) share similarities in the  
15 elemental ratios and concentrations for a given kind of inclusion (brine or vapor) in both garnet and  
16 quartz. The pyroxene-hosted brine and vapor inclusions show a higher spread of the data, probably  
17 reflecting the higher analytical uncertainty for this host mineral. For many elements, the ratio relative  
18 to Na are essentially identical for all fluid inclusion types and hosts at both locations (Figs. 10A-B).  
19 They are close to unity for K, and on the order of 0.1 for Pb; 0.01 for Zn, Rb, Sr, and Ba; 0.001 for B,  
20 S, As, Cs, W, and Bi; and 0.0001 for Ag, and Sb. In contrast, the ratios of Cu, Mo, and Au relative to  
21 Na vary up to an order of magnitude between the locations. They are higher in the Cu-rich periphery  
22 (0.01 Cu/Na, 0.005 Mo/Na, and 0.000005 Au/Na) than in the Au-Cu center (0.005 Cu/Na, 0.0001  
23 Mo/Na, and 0.000001 Au/Na). The ore metal contents also show higher scatter within fluid inclusion  
24 assemblages and samples when compared to other trace elements.  
25

26 In the deep barren core, ID inclusions from garnet and quartz show almost identical composition  
27 (Fig. 10C). The elemental ratios relative to Na for some elements (e.g. Li, B, Cu, As, Rb, Ag, Sb, Au,  
28 and Bi) in pyroxene-hosted inclusions are lower and more scattered than in garnet and quartz (Fig.  
29 10C). The ID inclusions in garnet and quartz show essentially identical elemental ratios for alkali and  
30 alkali earth metals, e.g. Li, B, Rb, Sr, Cs, Ba, when compared to the brine and vapor inclusions from  
31 the mineralized parts of the stock, but have notably higher Cu/Na (0.01–0.1) and Au/Na ratios  
32 (0.000005–0.00001). The Mo/Na ratios in quartz-hosted ID inclusions from the deep barren core are,  
33 however, comparable to those from the Au-Cu center. Occasional ID inclusions present in the upper  
34 parts of the deposit (lower section of the Cu-rich periphery) yield identical composition as their deep-  
35 seated equivalents.  
36

37 Only three secondary aqueous inclusions in calcite (AQ; < 10  $\mu\text{m}$ ) have been successfully  
38 analyzed, showing very low K/Na ratio, and low metal content (up to two orders of magnitude lower  
39 Zn, As, and Mo). The ore metals, i.e. Ag, Au, and Cu, and sulfur have not been detected in these  
40 fluids.  
41

## Interpretation and Discussion

In the following sections, we discuss the physical and chemical significance of the microthermometric and LA-ICP-MS data, followed by a comparison of fluid evolution in the skarn vs. the porphyry stockwork veins, concluding with some implications for ore deposition in these two contrasting host-rock environments.

### *Composition of the skarn-forming fluids*

Despite the nature of skarns, being products of carbonate-replacement by decarbonation, we did not observe CO<sub>2</sub> clathrate in fluid inclusions hosted by skarn minerals. Therefore we conclude that the CO<sub>2</sub> content of the fluid is low enough not to significantly contribute to freezing point depression and our interpretation of the microthermometric data (Hedenquist and Henley, 1985). This is in accordance with finding from other intrusion-related skarn deposits, where the CO<sub>2</sub> mol fraction of the fluids close to the endoskarn or in the center of the bodies is estimated to be below 0.1 (Einaudi, 1982). Example of Osgood Mountain and Ely skarn deposits (Nevada) suggest that the pyroxene, garnet and quartz depositing fluids had CO<sub>2</sub> mol fraction lower than 0.035 and 0.06, respectively. Only near marble contacts, the CO<sub>2</sub> content has been shown to fluctuate (Taylor and O'Neil, 1977).

Magmatic-hydrothermal solutions can contain significant amount of cations other than Na. Fluid inclusion and experimental studies show that FeCl<sub>2</sub>, KCl and NaCl can occur in similar concentrations in magmatic-hydrothermal fluids (e.g. Burnham, 1979; Eugster and Chou, 1979; Kouzmanov and Pokrovski, 2012). Destruction of the primary limestone at the expense of calc-silicate skarn minerals can also introduce Ca into the fluid. At Bingham Canyon, the LA-ICP-MS analysis revealed that the second most abundant cation in addition to Na in the skarn-forming fluids is K (Na/K up to 0.5). The Fe/Na ratio is variable but can be as high as 0.5, while the Ca/Na ratio, recorded in the quartz-hosted fluid inclusions, reaches up to 0.2. The apparent salinity of the fluid approximated by the H<sub>2</sub>O-NaCl system for any given ice melting temperature would differ from a true salinity in more realistic H<sub>2</sub>O-NaCl-KCl-CaCl<sub>2</sub>-FeCl<sub>2</sub> system (Steele-MacInnis et al., 2016). The difference in apparent salinity for the approximated H<sub>2</sub>O-NaCl (Bodnar, 1993) in comparison to, for example, H<sub>2</sub>O-NaCl-CaCl<sub>2</sub> system (Oakes et al., 1990) or H<sub>2</sub>O-NaCl-FeCl<sub>2</sub> system (Lecumberri-Sanchez et al., 2015) is, however, negligible for the range of salinities recorded in the vapor and ID inclusions (3–20 wt. % NaCl<sub>eq</sub>). Moreover, the chlorinity of the fluid remains nearly identical for the above described systems, as illustrated by the slope of ice liquidus for variable NaCl vs. CaCl<sub>2</sub> or FeCl<sub>2</sub> in the fluid (Fig. 11). This shows that conventional ice melting interpretation as wt. % NaCl<sub>eq</sub> provides a good approximation to total salinity in terms of equivalent Cl concentration, even though systematic errors are made in estimating Na concentration in the presence of significant fractions of divalent salts (e.g. CaCl<sub>2</sub>; Schlegel et al., 2012). The chlorinity of the skarn-hosted fluid inclusions reported in this study are likely to be close to their true values.

1  
2  
3  
4 *Composition of coeval fluid inclusions in different skarn minerals*  
5

6 In recent years, the issue of post-entrapment modification of quartz-hosted fluid inclusions  
7 emerged. Copper concentration in natural quartz-hosted vapor inclusions can be unusually high (e.g.  
8 Sawkins and Scherkenbach, 1981; Lowenstern et al., 1991; Mavrogenes et al., 2002) when compared  
9 to experimentally determined partition coefficients for copper in vapor relative to brine (Simon et al.,  
10 2006; Pokrovski et al., 2008; Frank et al., 2011). The experiments show that copper partitions  
11 preferentially into the brine while increasing sulfur fugacity in the system can allow limited amount of  
12 copper in the vapor. Re-equilibration experiments on quartz-hosted fluid and melt inclusions confirm  
13 that copper and also other monovalent cations of approx. 1 Å in size (i.e. H<sup>+</sup>, Li<sup>+</sup>, Na<sup>+</sup>, and Ag<sup>+</sup>),  
14 corresponding to the width of the structural channels along c-axis of quartz, can migrate between the  
15 vapor inclusions and their host (Zajacz et al., 2009; Li et al., 2009; Lerchbaumer and Audétat, 2012).  
16 The brine inclusions, however, stay largely unmodified. Copper can be enhanced up to three orders of  
17 magnitude in initially sulfur-rich and low-pH vapor inclusions, in exchange for H<sup>+</sup> loss. Studies on  
18 fluid inclusions from co-precipitating minerals other than quartz, e.g. topaz and beryl in Sn-W  
19 greisens (Seo and Heinrich, 2013; Schlöglova et al., 2017b) confirm the experimental results and offer  
20 more realistic data on copper content of magmatic vapors. Gold content of fluid inclusions is  
21 suggested to remain unchanged or represent minimum values, as Au would rather migrate outwards  
22 (Seo and Heinrich, 2013). There are, however, few data on gold content of natural vapors, owing to its  
23 generally low abundance in diluted low-density fluids and analytical limits.  
24  
25

26 Brine and vapor inclusions preserved in coexisting quartz, garnet and pyroxene at Bingham  
27 Canyon share common physical properties, i.e. homogenization temperatures and range of ice or salt  
28 melting temperatures, converted to salinities (Figs. 7, 12). Based on petrographic relations between  
29 the minerals, the entrapped fluids are likely to belong to temporally and compositionally similar  
30 hydrothermal stages, introduced just before sulfide precipitation (Fig. 3). Coexistence of nearly  
31 identical inclusion in various minerals thus allows a comparison of their chemical composition to test  
32 for post-entrapment modification. In particular, garnet is expected to be a more robust fluid inclusion  
33 host due its lower diffusivity when compared to quartz (Brady and Cherniak, 2010).  
34  
35

36 Inclusions in all the coexisting minerals show similar element to Na ratios within a given location  
37 in the deposit (Fig. 10). The Cu/Na ratio of the quartz-hosted vapor inclusions averages at 0.0025  
38 (~45 ppm Cu, calculated for average salinity of 5 wt. % NaCl<sub>eq</sub>) in the Au-Cu center and 0.020 (~255  
39 ppm Cu) at the Cu-rich periphery, compared to garnet-hosted vapors with 0.0029 (~35 ppm Cu) and  
40 0.015 (~80 ppm Cu), respectively, and pyroxene with 0.0016 (~110 ppm Cu). Observed differences  
41 are within analytical uncertainty and natural scatter of the data. Enhancement of Cu in the quartz-  
42 hosted vapor inclusions is therefore considered to be negligible. Likewise, Ag and Li content of the  
43 quartz-, garnet-, and pyroxene-hosted vapor inclusions in both locations (Au-Cu center and Cu-rich  
44 periphery) are nearly identical, averaging at 2·10<sup>-4</sup> Ag/Na in all minerals or 1.3–2.1 ppm Ag (quartz),  
45 1.9–2.2 ppm (garnet), 1.55 ppm (pyroxene); and 0.0015 Li/Na or 35 ppm Li (quartz), 55 ppm (garnet).  
46  
47

1  
2  
3  
4 Gold content of the vapor averages  $2 \cdot 10^{-6}$  Au/Na in all minerals and locations (corresponding to 2–  
5 130 ppb Au for inclusions in quartz, 13–19 ppb in garnet, and 48 ppb in pyroxene), except for the  
6 garnet-hosted vapors from the Au-Cu center with average of  $5 \cdot 10^{-7}$  Au/Na (scarce vapor inclusion in  
7 these samples where only three gold values have been recorded).  
8  
9

10 The pyroxene-hosted inclusions, although their salinities are similar to the garnet- and quartz-  
11 hosted equivalents (Fig. 10A), show higher scatter of the data and in the case of ID fluids, the trace  
12 element content is systematically lower. The data scatter might be attributed to imperfect host  
13 correction that propagates into the analytical results, as discussed above. The pyroxene might be also  
14 partly reacting with the fluids, as recorded by the highly saline brine inclusions that represent either  
15 very early hyper-saline fluids or have lost some of their water to the host, altering it to amphibole. The  
16 lower trace element content might be attributed to entrapment of an early Fe-poor diopside-forming  
17 fluid (*PXI*) partially modified by later fluid pulses causing recrystallization to Fe-rich diopside (*PX2*;  
18 e.g. Fig. 4E). The texture and microscale chemical variation of the pyroxene host might suggest that  
19 the pyroxene-hosted ID fluids represent a mixture of these different fluids. Generally, the pyroxene-  
20 hosted inclusions are the least constrained – hosted in commonly very dark and semi-transparent  
21 minerals of variable composition.  
22  
23

24 The Ag, Au, Cu, and Li contents of the vapor inclusions in quartz, garnet, and to some degree  
25 pyroxene, are nearly identical and therefore likely not affected by the post-entrapment modification.  
26 This can be explained by absence of a chemical potential gradient for the monovalent cations to  
27 migrate between the fluid inclusion and the host environment. This driving force is generally  
28 considered to be difference in H<sub>2</sub>S and H<sup>+</sup> activity between the (acidic) fluid in the inclusion and the  
29 immediate environment of the host (Lerchbaumer and Audétat, 2012). We propose that in the case of  
30 our samples, the acidic magmatic fluid outside of the crystals was neutralized upon reaction with  
31 carbonate to form skarn minerals. Therefore, the entrapped fluid does not have excess H<sup>+</sup> that would  
32 account for charge-balancing any incoming cations. Furthermore, sulfur – the element to bind any  
33 incoming copper in the case of post-entrapment modification thereof – is remarkably low in the fluid;  
34 below 1000 ppm as recorded in limited number of inclusions (< 10 %), compared to an average of  
35 ~10000 ppm S in the porphyry quartz stockwork (Seo et al., 2012). Therefore, in the case of the skarn-  
36 hosted inclusions, the interplay of the host rock and fluid chemistry does not create a favorable  
37 environment for any significant post-entrapment cation exchange, so that the composition of the fluid  
38 inclusions remain representative for the original skarn-forming fluids.  
39  
40

#### 51 *Fluid evolution in skarn and porphyry stockwork*

52 Skarn formation at Bingham Canyon was mainly driven by fluids associated with the intrusion of  
53 the QMP and LP, that was followed by two main stages of stockwork veining and Cu-Au  
54 mineralization extending into the earlier EM (Gruen et al., 2010; Landtwing et al., 2010; Redmond  
55 and Einaudi, 2010). Skarn formation cannot be attributed to the individual QMP and LP intrusions but  
56 overall was driven by the same evolving magmatic fluids.  
57  
58

The presence of intermediate-density inclusions in the deep barren core of the deposit (up to approx. 1000 m below the pre-mining surface, i.e. 3 km paleo-depth; Deino and Keith, 1997) is interpreted to represent a single-phase magmatic fluid that, upon further cooling and decompression, separated into brine and vapor fluids preserved in the upper part of the deposit (Redmond et al., 2004; Landtwing et al., 2010). In the skarn units from the barren core, this single-phase, intermediate-density fluid ( $\sim 0.6 \text{ g}\cdot\text{cm}^{-3}$ ) is preserved in the recrystallized pyroxene (*PX2*), andraditic garnet (*GRT2*), and quartz. The single-phase intermediate-density fluid entrapped at temperatures in excess of 500 °C and 800 bar (Fig. 12) are present in both the lithologies – skarn and porphyry stockwork – throughout the deep part of the deposit. Their apparent salinities, however, differ significantly (Figs. 7, 12). The ID fluids in the porphyry stockwork have average salinities of  $\sim 7 \text{ wt. \% NaCl}_{\text{eq}}$  determined from melting temperature of the CO<sub>2</sub> clathrate (Landtwing et al., 2010; Seo et al., 2012), compared to the average of 15 wt. % NaCl<sub>eq</sub> in the skarns. Redmond and Einaudi (2010) report occasional values as high as 13 wt. % total salinity in the porphyry quartz veins. The most likely explanation is mixing of intermediate-density fluids with earlier brines. The phase separation of the deep fluid could have produced an early volatile vapor and dense brine that, ponding in the deeper sections of the deposit, might have mixed and “up-salted” (cf. Blundy et al., 2015) the later ID fluids recorded in our study (Fig. 13). The higher salinity of the skarn-hosted ID inclusions is likely not a result of fluid-rock reaction as very low fluid to rock ratio (*F/R* < 0.001) would be required, the contrary to a high *F/R* typical for an ore-forming environment (Hennings et al., 2017).

The abrupt change in texture and composition from euhedral Al-poor andradite (*GRT2*) to Al-rich vein-like andradite (*GRT3*) is attributed to fracturing of the rock and phase separation of the ID fluid into highly saline brine (32–42 wt. % NaCl<sub>eq</sub>) and low-salinity vapor (2–7 wt. % NaCl<sub>eq</sub>,  $\sim 0.2 \text{ g}\cdot\text{cm}^{-3}$ ), under 420–380 °C and ca. 200 bar (Fig. 13). This may record the opening of rock permeability upon cooling of the magmatic-hydrothermal porphyry system during continued fluid flow, and a local change from near-lithostatic to hydrostatic pressure (Fig. 12). Consistently, the brine and vapor fluid inclusions are hosted in the Fe-rich diopside (*PX2*), Al-rich andradite (*GRT3*) and quartz, and only in the upper part of the deposit. The formation of garnet, quartz and calcite are all associated with the main skarn stage alteration and described to be contemporaneous with the sulfide deposition (e.g. Atkinson and Einaudi, 1978). However, petrographic relations (Fig. 5) indicate that garnet and quartz have formed rather shortly prior to the major pyrite and chalcopyrite precipitation, followed by calcite. Therefore, the vapor and brine inclusions therefore record fluids entrapped before the sulfide mineralization in the skarns.

The physico-chemical properties of the brine inclusions in skarns are nearly identical in the center and the periphery of the deposit. Their salinities and homogenization temperatures correspond to conditions recorded by the brines at the periphery of the porphyry stockwork (430–370 °C at  $\sim 200$  bar; Fig. 12). In the quartz stockwork, the increasing salinity of the brines – from ca. 35 wt. % NaCl<sub>eq</sub> at the deeper flanks of the copper ore body to ca. 55 wt. % NaCl<sub>eq</sub> in the cupola of the bell-shaped ore

body – is attributed to widening of the solvus during decompression but only slight temperature drop (Landtwing et al., 2010).

The ID, brine, and vapor inclusions in the porphyry stockwork are hosted in several generations of quartz veins distinguished by specific response in cathode luminescence; the bright Q1 quartz, partly dissolved and overgrown by dull, fracture-filling Q2 quartz that is associated with sulfide mineralization (Fig. 3; Landtwing, 2004). Later generation of Q3 quartz associated with sericite alteration but protracted sulfide precipitation preserves aqueous, low salinity fluids. These aqueous fluids might have an analog in the skarns, as rare and very small calcite-hosted aqueous inclusions that lack the ore metals and have lower content of some trace elements.

Trace element composition in the fluids from skarns and porphyry stockwork are similar within analytical uncertainty for K, Fe, Rb but remarkably different for B, Cs, S, and metals, especially Ag, Au, Cu, and Mo (Fig. 14). Depletion of boron content in the skarn-hosted fluids might be attributed to early precipitation of a Ca-borosilicate phase (e.g. danburite, datolite) that might have been overlooked in the complex skarn samples. Strontium content of the skarn-hosted fluids is elevated likely due to initially high Sr content of the limestone (Brand et al., 1998). Cesium, on the other hand, is an incompatible element retained and enriched in the fluid, alike lead and zinc. Pb-Zn ores can be found in the porphyry stock, outside of the copper ore shell, while in the skarn and also hornfels, galena and sphalerite can be found as microscopic inclusions in late hydrous phases, e.g. amphibole. The difference in S and metal contents between skarn and porphyry fluids is discussed in the section below.

#### *Metal precipitation in skarn and porphyry stockwork*

The most significant difference between porphyry- and skarn-hosted fluids was recorded for sulfur and copper (Figs. 14, 15A). The sulfur to sodium ratio close to 1 for vapor in the porphyry drops to values below 0.001 S/Na in the skarn. This relationship is also observed for copper: in the porphyry stockwork, average Cu/Na ratios are ~1 for vapor and ~0.1 for brine, whereas in the skarns, they are ~0.008 in vapor and ~0.005 in brine. The S to Cu ratio in the skarn-hosted fluids (Fig. 15C) is, however, still in favor of sulfur, driving the precipitation of Cu-sulfides. The difference in Ag, Au and Mo is also profound: half an order of magnitude for Ag/Na and over and order of magnitude for Au/Na and Mo/Na.

It should be noted that Cu content of the vapor inclusions from the porphyry stockwork are exceptionally high and the inclusions in this environment have probably suffered a post-entrapment modification. Additionally, the Au analyses from the porphyry stockwork should be regarded with caution since the rather rare values are close to their detection limits.

The lower sulfur and metal content of the skarn fluids can be explained by extensive chalcopyrite precipitation from the hot fluids in the porphyry stockwork (Fig. 15B). The skarn-hosted sulfides were either precipitated from this rather depleted fluid, or from a later, metal-rich fluid batch, potentially

related to the emplacement of the youngest porphyry units (LP). The principal sulfide mineralization in the skarn, on microscale, appears to be rather a “single” event comparing to repeated and crosscutting veining in the porphyry stockwork. Cu-Pb-Zn chemical systematics of the porphyry and skarn fluids (Fig. 15B) support the first hypothesis. Indeed, the precipitation of Cu-sulfides in the porphyry stockwork leads to depletion of Cu in the fluids, while keeping the Pb/Zn ratio constant (Fig. 15B). The composition of the fluids in the skarns lie at the low-Cu end of the porphyry trend, and in addition, show highly variable Pb/Zn ratios. This suggests that the fluid inclusions in the skarns represent fluids already exhausted in much of the original Cu and S by the crystallization of Cu-sulfides in the porphyry stockwork, but show variable Zn and Pb concentrations due to different degrees of incipient galena and sphalerite precipitation in the skarns. Galena and sphalerite have been observed as microscopic inclusions in the skarn minerals and are present as ore in the surrounding hornfels units.

Despite the lower amount of sulfur and ore metals in the skarn-hosted fluids compared with the porphyry-hosted fluids, the skarns have slightly higher Cu and Au grades, at similar Au/Cu ratio. (Fig. 15A). The high ore grades in the skarn are not an exceptional feature and have been reported from other porphyry-related skarn deposits (summarized in Einaudi, 1982). The precipitation of copper sulfides in the porphyry stock at Bingham was facilitated by progressive cooling of the fluid and its separation into brine and vapor upon change into hydrostatic regime (Redmond et al., 2004; Landtwing et al., 2005; Weis et al., 2012). Fluid evolution in the skarns has differed greatly from that in the porphyry veins. The main difference in the skarns is the chemical reactivity of the calcareous protolith (e.g. Meinert et al., 2005; Reed and Palandri, 2006), possibly aided by more intense fracturing (Einaudi, 1982). The higher metal grade but lower concentration of metals and sulfur in the fluids are most easily explained by greater efficiency of ore mineral precipitation on the scale of skarn orebodies, although on the sample scale, chalcopyrite is texturally later compared to the inclusion-bearing calc-silicate minerals. This apparent contradiction is unresolved but similar to the timing situation in stockwork veins: on the large scale ore grade correlates with quartz vein density (Gruen et al., 2010; Redmond and Einaudi, 2010) but on the microscale of vein samples the bulk of quartz is earlier than the precipitation of chalcopyrite (Redmond et al., 2004; Landtwing et al., 2005).

## Conclusions and Outlook

Our study brings new analytical data for trace element and metal content of fluid inclusions hosted by complex calc-silicate minerals. Pyroxene, garnet and quartz, formed during early and main stage alteration of skarn at Bingham Canyon, preserve intermediate-density fluid inclusions mostly in the deeper parts of the system, and brine and vapor inclusions in the upper parts of the orebody. This spatial variation closely matches the spatial distribution of fluid inclusion types in the porphyry stockwork veins described in previous studies, showing that fluids in both lithologies followed a similar pressure-temperature path during ascent. The preservation of coeval inclusions in the skarn minerals allowed an assessment of the extent of their post-entrapment modification. Overlapping trace

1  
2  
3  
4 element concentrations in brine and vapor inclusions hosted by coexisting quartz and garnet suggest  
5 that the inclusions in both minerals did not suffer significant modification, and that their compositions  
6 are representative of the original fluid. The intermediate-density, brine and vapor inclusions in the  
7 Bingham skarns share similar trace element chemistry with fluids present in the porphyry quartz  
8 stockwork, with exception of their sulfur and ore metal content (i.e. Ag, Au, Cu and Mo). Precise  
9 timing of the skarn vs. porphyry mineralization is, however, unclear. Evidence of depleted metal  
10 content of the skarn-hosted fluids, in contrast to skarn bodies hosting comparable or even higher ore  
11 grades, indicate effective sulfide precipitation by intense fluid-rock reaction, aided by pH  
12 neutralization of the magmatic fluid. In addition, the brittle behavior of skarns and likely volume loss  
13 during alteration facilitated high density of veining and intense fluid-rock reaction.  
14

15 Topics for further research should include improvement in the reduction of LA-ICP-MS analytical  
16 data for fluid inclusions in complex host minerals. The use of apparent salinity (wt. % NaCl<sub>eq</sub>) as  
17 internal standard for fluids with more complex composition introduces systematic error and elemental  
18 concentrations returned by this method are likely to be overestimated, but cannot be readily corrected  
19 due to the presence of major elements in most minerals other than quartz. A data reduction method  
20 using an apparent chlorinity (ppm Cl) as an internal standard could return more realistic results,  
21 however, accurate analysis of chlorine by LA-ICP-MS is required. Spatial and temporal relation of  
22 ore formation in the porphyry stockwork comparing to the skarns remains unclear and more rigorous  
23 sampling and detailed observations at the contacts between the two lithologies is suggested.  
24

### 33 Acknowledgements

34 We acknowledge the financial support by the Swiss National Science Foundation (SNF/Project  
35 200021-146651) and cooperation with the Kennecott Utah Copper Corp. (Kim Schroeder). We thank  
36 Marcel Guillong for discussions about the LA-ICP-MS data reduction strategies and Larry Meinert for  
37 his initial comments and editorial guidance during the revision of the original manuscript.  
38  
39  
40  
41  
42  
43  
44  
45  
46  
47  
48  
49  
50  
51  
52  
53  
54  
55  
56  
57  
58  
59  
60  
61  
62  
63  
64  
65

## References

- Atkinson, W.W., 1975, Alteration and mineralization in surface exposures at Carr Fork, Bingham District, Utah, in Bray, R.E., and Wilson, J.C., eds., Guide Book to the Bingham Mining District: Bingham Canyon, Utah, Kennecott Utah Copper Corporation, p. 119-133.
- Atkinson, W.W., and Einaudi, M.T., 1978, Skarn formation and mineralization in contact aureole at Carr Fork, Bingham, Utah: Economic Geology, v. 73, p. 1326-1365.
- Ault, K.M., 2004, Geochemistry, physico-chemical controls, and genesis of the El Mochito Zn-Pb-Ag skarn-hosted deposit, Honduras: Unpublished Ph.D. Thesis, McGill University, 238 p.
- Babcock, R.C., Ballantyne, G.H., and Phillips, C.H., 1995, Summary of the geology of the Bingham district, Utah: Arizona Geological Society Digest, v. 20, p. 316-335.
- Baker, T., and Lang, J.R., 2003, Reconciling fluid inclusion types, fluid processes, and fluid sources in skarns: an example from the Bismark Deposit, Mexico: Mineralium Deposita, v. 38, p. 474-495.
- Baker, T., Van Achterberg, E., Ryan, C.G., and Lang, J.R., 2003, PIXE analysis of skarn ore fluids Bismark, Mexico: Mineral Exploration and Sustainable Development, v. 1-2, p. 227-230.
- Beeson, J.J., 1917, The disseminated copper ores of Bingham Canyon, Utah: Transactions of the American Institute of Mining Engineers, v. 54, p. 356-401.
- Bertelli, M., Baker, T., Cleverley, J.S., and Ulrich, T., 2009, Geochemical modelling of a Zn-Pb skarn: Constraints from LA-ICP-MS analysis of fluid inclusions: Journal of Geochemical Exploration, v. 102, p. 13-26.
- Blundy, J., Mavrogenes, J., Tattitch, B., Sparks, S., and Gilmer, A., 2015, Generation of porphyry copper deposits by gas-brine reaction in volcanic arcs: Nature Geoscience, v. 8, p. 235-240.
- Bodnar, R.J., 1993, Revised equation and table for determining the freezing-point depression of H<sub>2</sub>O-NaCl solutions: Geochimica et Cosmochimica Acta, v. 57, p. 683-684.
- Bodnar, R.J., Lecumberri-Sanchez, P., Moncada, D., and Steele-MacInnis, M., 2014, Fluid inclusions in hydrothermal ore deposits, in Holland, H., and Turekian, K., eds., Treatise on Geochemistry, 2nd ed.: Oxford, Elsevier, p. 119-142.
- Boutwell, J.M., 1905, Genesis of the ore-deposits at Bingham, Utah: Transactions of the American Institute of Mining and Metallurgical Engineers, v. 36, p. 541-580.
- Brady, J.B., and Cherniak, D.J., 2010, Diffusion in minerals: an overview of published experimental diffusion data: Reviews in Mineralogy and Geochemistry, v. 72, p. 899-920.
- Brand, U., Morrison, J.O., and Campbell, I.T., 1998, Strontium in sedimentary rocks, Geochemistry: Dordrecht, Springer Netherlands, p. 600-603.
- Burnham, C.W., 1979, Magmas and hydrothermal fluids, in Barnes, H.L., ed., Geochemistry of hydrothermal ore deposits: New York, John Wiley and Sons, p. 71-136.
- Butler, B.S., Loughlin, G.S., and Heikes, V.C., 1920, The ore deposits of Utah: U.S. Geological Survey Professional Paper, v. 111, 672 p.
- Cameron, D.E., and Garmoe, W.J., 1987, Geology of skarn and high-grade gold in the Carr Fork Mine, Utah: Economic Geology, v. 82, p. 1319-1333.
- Catchpole, H., Kouzmanov, K., Bendezu, A., Ovtcharova, M., Spikings, R., Stein, H., and Fontbote, L., 2015, Timing of porphyry (Cu-Mo) and base metal (Zn-Pb-Ag-Cu) mineralisation in a magmatic-hydrothermal system-Morococha district, Peru: Mineralium Deposita, v. 50, p. 895-922.
- De Kalb, C., 1909, The Utah copper mine: Mining and Scientific Press, v. 98, p. 516-521.
- Deino, A., and Keith, J.D., 1997, Ages of volcanic and intrusive rocks in the Bingham mining district, Utah: Society of Economic Geologists Guidebook Series, v. 29, p. 91-100.
- Dilles, J.H., 1987, Petrology of the Yerington Batholith, Nevada - evidence for evolution of porphyry copper ore fluids: Economic Geology, v. 82, p. 1750-1789.
- Driesner, T., and Heinrich, C.A., 2007, The system H<sub>2</sub>O-NaCl. Part I: Correlation formulae for phase relations in temperature-pressure-composition space from 0 to 1000 degrees C, 0 to 5000 bar, and 0 to 1 X-NaCl: Geochimica et Cosmochimica Acta, v. 71, p. 4880-4901.
- Einaudi, M.T., 1982, Description of skarns associated with porphyry copper plutons, in Titley, S.R., ed., Advances in geology of the porphyry copper deposits: southwestern North America: Tucson, Arizona, The university of Arizona Press, p. 139-184.
- Einaudi, M.T., Moore, W.J., and Wilson, J.C., 1978, An issue devoted to the Bingham mining district: Economic Geology, v. 73, p. 1215-1217.
- Eugster, H.P., and Chou, I.M., 1979, Model for the deposition of Cornwall-type magnetite deposits: Economic Geology, v. 74, p. 763-774.
- Fekete, S., Weis, P., Driesner, T., Bouvier, A. S., Baumgartner, L., and Heinrich, C.A., 2016, Contrasting hydrological processes of meteoric water incursion during magmatic-hydrothermal ore deposition: An oxygen isotope study by ion microprobe: Earth and Planetary Science Letters, v. 451, p. 263-271.
- Field, C.W., and Moore, W.J., 1971, Sulfur Isotope study of 'B' limestone and Galena fissure ore deposits of the U.S. Mine, Bingham mining district, Utah: Economic Geology, v. 66, p. 48-62.
- Frank, M.R., Simon, A.C., Pettke, T., Candela, P.A., and Piccoli, P.M., 2011, Gold and copper partitioning in magmatic-hydrothermal systems at 800 degrees C and 100 MPa: Geochimica et Cosmochimica Acta, v. 75, p. 2470-2482.

- Graham, S., Pearson, N., Jackson, S., Griffin, W., and O'Reilly, S.Y., 2004, Tracing Cu and Fe from source to porphyry: in situ determination of Cu and Fe isotope ratios in sulfides from the Grasberg Cu-Au deposit: *Chemical Geology*, v. 207, p. 147-169.
- Grew, E.S., Locock, A.J., Mills, S.J., Galuska, I.O., Galuskin, E.V., and Halenius, U., 2013, Nomenclature of the garnet supergroup: *American Mineralogist*, v. 98, p. 785-810.
- Gruen, G., Heinrich, C.A., and Schroeder, K., 2010, The Bingham Canyon porphyry Cu-Mo-Au deposit. II. Vein geometry and ore shell formation by pressure-driven rock extension: *Economic Geology*, v. 105, p. 69-90.
- Guillong, M., Meier, D. L., Allan, M.M., Heinrich, C.A., and Yardley, B.W.D., 2008, SILLS: A Matlab-based program for the reduction of laser ablation ICP-MS data of homogeneous materials and inclusions: *Mineralogical Association of Canada, Short Course Series*, v. 40, p. 323-333.
- Hansen, L.A., 1961, The stratigraphy of the Carr fork mines, Bingham mining district, Bingham, Utah: *Utah Geological and Mineralogical Survey, Guidebook to the Geology of Utah*, v. 16, p. 71-81.
- Haynes, F.M., 1985, Determination of fluid inclusion compositions by sequential freezing: *Economic Geology*, v. 80, p. 1436-1439.
- Haynes, F.M., and Kesler, S.E., 1988, Compositions and sources of mineralizing fluids for chimney and manto limestone-replacement ores in Mexico: *Economic Geology*, v. 83, p. 1985-1992.
- Hedenquist, J.W., and Henley, R.W., 1985, The Importance of CO<sub>2</sub> on freezing-point measurements of fluid inclusions - evidence from active geothermal systems and implications for epithermal ore deposition: *Economic Geology*, v. 80, p. 1379-1406.
- Heinrich, C.A., Günther, D., Audéat, A., Ulrich, T., and Frischknecht, R., 1999, Metal fractionation between magmatic brine and vapor, determined by microanalysis of fluid inclusions: *Geology*, v. 27, p. 755-758.
- Hemley, J.J., and Hunt, J.P., 1992, Hydrothermal ore-forming processes in the light of studies in rock-buffered systems: II. Some general geologic applications: *Economic Geology*, v. 87, p. 23-43.
- Hennings, S.K., Wagner, T., Ulmer, P., and Heinrich, C.A., 2017, Fluid evolution of the Monte Mattoni Mafic Complex, Adamello Batholith, Northern Italy: insights from fluid inclusion analysis and thermodynamic modeling: *Journal of Petrology*, v. 58, p. 1645-1670.
- Hunt, R.N., 1924, The ores in the limestones at Bingham, Utah: *Transactions of the American Institute of Mining and Metallurgical Engineers*, v. 70, p. 856-883.
- Inan, E.E., and Einaudi, M.T., 2002, Nukundamite (Cu<sub>3.38</sub>Fe<sub>0.62</sub>S<sub>4</sub>)-bearing copper ore in the Bingham Porphyry Deposit, Utah: Result of upflow through quartzite: *Economic Geology*, v. 97, p. 499-515.
- Irwin, J.J., and Roedder, E., 1995, Diverse origins of fluid in magmatic inclusions at Bingham (Utah, USA), Butte (Montana, USA), St-Austell (Cornwall, UK), and Ascension-Island (Mid-Atlantic, UK), Indicated by Laser Microprobe Analysis of Cl, K, Br, I, Ba Plus Te, U, Ar, Kr, and Xe: *Geochimica et Cosmochimica Acta*, v. 59, p. 295-312.
- James, A.H., Smith, W.H., and Bray, R.E., 1961a, Bingham district: a zoned porphyry ore deposit: *in* Cook, D.R., ed., *Geology of the Bingham mining district and northern Oquirrh Mountains: Utah Geological Survey, Guidebook to the Geology of Utah*, v. 16, p. 81-100.
- James, A.H., Smith, W.H., and Welsh, J.E., 1961b, General geology and structure of the Bingham District, Utah, *in* Cook, D.R., ed., *Geology of the Bingham mining district and northern Oquirrh Mountains: Utah Geological Survey, Guidebook to the Geology of Utah*, v. 16, p. 49-71.
- James, L.P., 1978, Bingham copper deposits, Utah, as an exploration target; history and pre-excavation geology: *Economic Geology*, v. 73, p. 1218-1227.
- John, D.A., 1989, Geologic setting, depths of emplacement, and regional distribution of fluid inclusions in intrusions of the central Wasatch Mountains, Utah: *Economic Geology*, v. 84, p. 386-409.
- John, D.A., and Ballantyne, G.H., eds, 1997, *Geology and ore deposits of the Oquirrh and Wasatch Mountains, Utah: Society of Economic Geologists, Guidebook Series*, v. 29, 256 p.
- Johnson, M.G., 1973, Placer gold deposits of Utah: *Bulletin of the U.S. Geological Survey*, v. 1357, 26 p.
- Jowitt, S.M., Mudd, G.M., and Weng, Z., 2013, Hidden mineral deposits in Cu-dominated porphyry-skarn systems: how resource reporting can occlude important mineralization types within mining camps. *Economic geology, Scientific Communicatinis*, v. 108, p. 1185-1193.
- Kendrick, M.A., Burgess, R., Patrck, R.A.D., and Turner, G., 2001a, Fluid inclusion noble gas and halogen evidence on the origin of Cu-Porphyry mineralising fluids: *Geochimica et Cosmochimica Acta*, v. 65, p. 2651-2668.
- Kendrick, M.A., Burgess, R., Patrck, R.A.D., and Turner, P.G., 2001b, Halogen and Ar-Ar age determinations of inclusions within quartz veins from porphyry copper deposits using complementary noble gas extraction techniques: *Chemical Geology*, v. 177, p. 351-370.
- Kloppenburg, A., Grocott, J., and Hutchinson, D., 2010, Structural setting and synplutonic fault kinematics of a Cordilleran Cu-Au-Mo porphyry mineralization system, Bingham mining district, Utah: *Economic Geology*, v. 105, p. 743-761.
- Kouzmanov, K., and Pokrovski, G.S., 2012, Hydrothermal controls on metal distribution in porphyry Cu (-Mo-Au) systems: *Economic Geology, Special Publication*, v. 16, p. 573-618.
- Krahulec, K., 2010, Production history of the Bingham mining district, Salt Lake City, Utah, *in* Krahulec, K., and Schroeder, K., eds., *Tops and bottoms of porphyry copper deposits: the Binhgam and Southwest Tintic districts, Utah: Society of Economic Geologists, Guidebook Series*, v. 41, p. 25-33.
- Kwak, T.A.P., 1986, Fluid inclusions in skarns (carbonate replacement deposits): *Journal of metamorphic Geology*, v. 4, p. 363-384.

- Kwak, T.A.P., and Tan, T.H., 1981, The importance of  $\text{CaCl}_2$  in fluid composition trends - evidence from the King Island (Dolphin) skarn deposit: *Economic Geology*, v. 76, p. 955-960.
- Landtwing, M.R., 2004, Fluid evolution and ore metal precipitation at the Bingham porphyry Cu-Au-Mo deposit, Utah, deduced from cathodoluminescence imaging and LA-ICPMS microanalysis of fluid inclusions: Unpublished Ph.D. thesis, ETH Zurich, 126 p.
- Landtwing, M.R., Furrer, C., Redmond, P.B., Pettke, T., Guillong, M., and Heinrich, C.A., 2010, The Bingham Canyon porphyry Cu-Mo-Au deposit. III. Zoned copper-gold ore deposition by magmatic vapor expansion: *Economic Geology*, v. 105, p. 91-118.
- Landtwing, M.R., Heinrich, C.A., Halter, W.E., Pettke, T., Redmond, P.B., and Einaudi, M.T., 2002, Fluid evolution at the Bingham Cu-Au-Mo-Ag porphyry deposit: *Geochimica et Cosmochimica Acta*, v. 66, p. A430.
- Landtwing, M.R., Pettke, T., Halter, W.E., Heinrich, C.A., Redmond, P.B., Einaudi, M.T., and Kunze, K., 2005, Copper deposition during quartz dissolution by cooling magmatic-hydrothermal fluids: The Bingham porphyry: *Earth and Planetary Science Letters*, v. 235, p. 229-243.
- Lanier, G., John, E.C., Swensen, A.J., Reid, J., Bard, C.E., Caddey, S.W., and Wilson, J.C., 1978, General geology of Bingham Mine, Bingham Canyon, Utah: *Economic Geology*, v. 73, p. 1228-1241.
- Large, S.J.E., Bakker, E.Y.N., Weis, P., Wölle, M., Ressel, M., and Heinrich, C.A., 2016, Trace elements in fluid inclusions of sediment-hosted gold deposits indicate a magmatic-hydrothermal origin of the Carlin ore trend: *Geology*, v. 44, p. 1015-1018.
- Lecumberri-Sánchez, P., Steele-MacInnis, M., and Bodnar, R.J., 2012, A numerical model to estimate trapping conditions of fluid inclusions that homogenize by halite disappearance: *Geochimica et Cosmochimica Acta*, v. 92, p. 14-22.
- Lecumberri-Sánchez, P., Steele-MacInnis, M., and Bodnar, R.J., 2015, Synthetic fluid inclusions XIX. Experimental determination of the vapor-saturated liquidus of the system  $\text{H}_2\text{O}-\text{NaCl}-\text{FeCl}_2$ : *Geochimica et Cosmochimica Acta*, v. 148, p. 34-49.
- Lerchbaumer, L., and Audéat, A., 2012, High Cu concentrations in vapor-type fluid inclusions: An artifact?: *Geochimica et Cosmochimica Acta*, v. 88, p. 255-274.
- Li, Y., Audéat, A., Lerchbaumer, L., and Xiong, X.L., 2009, Rapid Na, Cu exchange between synthetic fluid inclusions and external aqueous solutions: evidence from LA-ICP-MS analysis: *Geofluids*, v. 9, p. 321-329.
- Lindgren, W., 1924, Contact metamorphism at Bingham, Utah: *Bulletin of the Geological Society of America*, v. 35, p. 507-534.
- Lowenstern, J.B., Mahood, G.A., Rivers, M.L., and Sutton, S.R., 1991, Evidence for extreme partitioning of copper into magmatic vapour phase: *Science*, v. 252, p. 1405-1408.
- Mavrogenes, J.A., Berry, A.J., Newville, M., and Sutton, S.R., 2002, Copper speciation in vapor-phase fluid inclusions from the Mole Granite, Australia: *American Mineralogist*, v. 87, p. 1360-1364.
- Meinert, L. D., Hedenquist, J.W., Satoh, H., and Matsuhisa, Y., 2003, Formation of anhydrous and hydrous skarn in Cu-Au ore deposits by magmatic fluids: *Economic Geology*, v. 98, p. 147-156.
- Meinert, L.D., Dipple, G.M., Niculescu, S., Hedenquist, J.W., Thompson, J.F.H., Goldfarb, R.J., and Richards, J.P., 2005, World skarn deposits, in Hedenquist, J.W., Thompson, J.F.H., Goldfarb, R.J., and Richards, J.P., eds., *Economic Geology 100th Anniversary Volume*: Society of Economic Geologists, Littleton CO, p. 299-336.
- Morimoto, N., Fabries, J., Ferguson, A.K., Ginzburg, I.V., Ross, M., Seifert, F.A., Zussman, J., Aoki, K., and Gottardi, G., 1988, Nomenclature of pyroxenes: *American Mineralogist*, v. 73, p. 1123-1133.
- Nash, J.T., 1976, Fluid-inclusion petrology: data from porphyry copper deposits and application to exploration: U.S. Geological Survey Professional Paper, v. 907 D, p. 1-16.
- Oakes, C.S., Bodnar, R.J., and Simonson, J.M., 1990, The system  $\text{NaCl}-\text{CaCl}_2-\text{H}_2\text{O}$ : I. The ice liquidus at 1 Atm total pressure: *Geochimica et Cosmochimica Acta*, v. 54, p. 603-610.
- Parry, W.T., Wilson, P.N., Moser, D., and Heizler, M.T., 2001, U-Pb dating of zircon and 40Ar/39Ar dating of biotite at Bingham, Utah: *Economic Geology*, v. 96, p. 1671-1683.
- Peng, H.J., Zhang, C.Q., Mao, J.W., Santosh, M., Zhou, Y.M., and Hou, L., 2015, Garnets in porphyry-skarn systems: A LA-ICP-MS, fluid inclusion, and stable isotope study of garnets from the Hongniu-Hongshan copper deposit, Zhongdian area, NW Yunnan Province, China: *Journal of Asian Earth Sciences*, v. 103, p. 229-251.
- Phillips, C.H., Smith, T.W., and Harrison, E.D., 1998, Alteration, metal zoning, and ore controls in the Bingham Canyon porphyry copper deposit, Utah: *Society of Economic Geologists, Guidebook Series*, v. 29, p. 133-145.
- Pokrovski, G.S., Borisova, A.Y., and Harrichoury, J.C., 2008, The effect of sulfur on vapor-liquid fractionation of metals in hydrothermal systems: *Earth and Planetary Science Letters*, v. 266, p. 345-362.
- Pollard, P.J., 2014, Grade distribution of the Giant OK Tedi Cu-Au deposit, Papua New Guinea: A discussion: *Economic Geology*, v. 109, p. 1489-1492.
- Porter, J.C., Schroeder, K., and Austin, G., 2012, Geology of the Bingham Canyon porphyry Cu-Mo-Au deposit, Utah: *Society of Economic Geologists, Special Publication*, v. 16, p. 127-144.
- Proffett, J.M., 2009, High Cu grades in porphyry Cu deposits and their relationship to emplacement depth of magmatic sources: *Geology*, v. 37, p. 675-678.
- Redmond, P.B., and Einaudi, M.T., 2010, The Bingham Canyon porphyry Cu-Mo-Au deposit. I. Sequence of intrusions, vein formation, and sulfide deposition: *Economic Geology*, v. 105, p. 43-68.
- Redmond, P.B., Einaudi, M.T., Inan, E.E., Landtwing, M.R., and Heinrich, C.A., 2004, Copper deposition by fluid cooling in intrusion-centered systems: New insights from the Bingham porphyry ore deposit, Utah: *Geology*, v. 32, p. 217-220.

- Reed, M.H., and Palandri, J., 2006, Sulfide mineral precipitation from hydrothermal fluids: *Reviews in Mineralogy and Geochemistry*, v. 61, p. 609-631.
- Reid, J.E., 1978, Skarn alteration of Commercial Limestone, Carr Fork area, Bingham, Utah: *Economic Geology*, v. 73, p. 1315-1325.
- Rio Tinto 2017 Annual report: [http://www.riotinto.com/documents/RT\\_2017\\_annual\\_report.pdf](http://www.riotinto.com/documents/RT_2017_annual_report.pdf), 258 p.
- Roedder, E., 1971, Fluid inclusion studies on porphyry-type ore deposits at Bingham, Utah, Butte, Montana, and Climax, Colorado: *Economic Geology*, v. 66, p. 98-120.
- Roedder, E., 1984, Fluid inclusions, in Ribbe, P.H., ed., *Reviews in Mineralogy*, Mineralogical Society of America, v. 12, p. 646.
- Rottier, B., Rezeau, H., Casanova, V., Kouzmanov, K., Moritz, R., Schläglova, K., Wölle, M., and Fontbote, L., 2017, Trace element diffusion and incorporation in quartz during heating experiments: *Contributions to Mineralogy and Petrology*, v. 172.
- Rubright, R.D., and Hart, O.J., 1968, Non-porphyry ores of the Bingham district, Utah, in Ridge, J.D., ed., *Ore Deposits of the United States*: New York, AIME, v. 1, p. 886-907.
- Samson, I.M., Williams-Jones, A.E., Ault, K.M., Gagnon, J.E., and Fryer, B.J., 2008, Source of fluids forming distal Zn-Pb-Ag skarns: Evidence from laser ablation-inductively coupled plasma-mass spectrometry analysis of fluid inclusions from El Mochito, Honduras: *Geology*, v. 36, p. 947-950.
- Sawkins, F.J., and Scherkenbach, D.A., 1981, High copper content of fluid inclusions in quartz from northern Sonora: Implications for ore-genesis theory: *Geology*, v. 9, p. 37-40.
- Schlegel, T.U., Wölle, M., Steele-MacInnis, M., and Heinrich, C.A., 2012, Accurate and precise quantification of major and trace element compositions of calcic-sodic fluid inclusions by combined microthermometry and LA-ICPMS analysis: *Chemical Geology*, v. 334, p. 144-153.
- Schläglova, K., Wölle, M., and Heinrich, C.A., 2017a, LA-ICP-MS analysis of fluid inclusions: contamination effects challenging micro-analysis of elements close to their detection limit: *Journal of Analytical Atomic Spectrometry*, v. 32, p. 1052-1063.
- Schläglova, K., Wölle, M., Heinrich, C.A., and Dolejš, D., 2017b, Copper, gold, and bismuth behavior in magmatic-hydrothermal systems: *Mineral Resources to Discover, Proceedings of the SGA 14th Biennial Meeting*, Québec City, Canada, v. 1, p. 95-98.
- Seo, J.H., Guillong, M., and Heinrich, C.A., 2012, Separation of molybdenum and copper in porphyry deposits: The roles of sulfur, redox, and pH in ore mineral deposition at Bingham Canyon: *Economic Geology*, v. 107, p. 333-356.
- Seo, J.H., and Heinrich, C.A., 2013, Selective copper diffusion into quartz-hosted vapor inclusions: Evidence from other host minerals, driving forces, and consequences for Cu-Au ore formation: *Geochimica et Cosmochimica Acta*, v. 113, p. 60-69.
- Sheppard, S.M., Nielsen, R.L., and Taylor, H.P., 1971, Hydrogen and oxygen isotope ratios in minerals from porphyry copper deposits: *Economic Geology*, v. 66, p. 515-542.
- Sillitoe, R.H., 2010, Porphyry copper systems: *Economic Geology*, v. 105, p. 3-41.
- Simon, A.C., Pettke, T., Candela, P.A., Piccoli, P.M., and Heinrich, C.A., 2006, Copper partitioning in a melt-vapor-brine-magnetite-pyrrhotite assemblage: *Geochimica et Cosmochimica Acta*, v. 70, p. 5583-5600.
- Smith, W.H., 1975, A short history of the Bingham Mining District, in Bray, R.E., and Wilson, J.C., eds., *Guide book to the Bingham Mining District: Society of Economic Geologists, Guidebook series*, p. 3-20.
- Spencer, E.T., Wilkinson, J.J., Nolan, J., and Berry, A.J., 2015, The controls of post-entrapment diffusion on the solubility of chalcopyrite daughter crystals in natural quartz-hosted fluid inclusions: *Chemical Geology*, v. 412, p. 15-25.
- Stacey, J.S., Moore, W.J., and Rubright, R.D., 1967, Precision measurement of lead isotopes ratios: preliminary analyses from the U.S. mine, Bingham Canyon, Utah: *Earth and Planetary Science Letters*, v. 2, p. 489-499.
- Starkins, R.D., 1983, Fluid inclusion study of the Carr Fork skarn deposit, Bingham Mining District, Utah, Unpublished M.Sc. Thesis, Boston State College, 134 p.
- Steele-MacInnis, M., Bodnar, R.J., and Naden, J., 2011, Numerical model to determine the composition of  $H_2O-NaCl-CaCl_2$  fluid inclusions based on microthermometric and microanalytical data: *Geochimica et Cosmochimica Acta*, v. 75, p. 21-40.
- Steele-MacInnis, M., Lecumberri-Sánchez, P., and Bodnar, R.J., 2012, HokieFlincs\_H<sub>2</sub>O-NaCl: A Microsoft Excel spreadsheet for interpreting microthermometric data from fluid inclusions based on the PVTX properties of H<sub>2</sub>O-NaCl: *Computers & Geosciences*, v. 49, p. 334-337.
- Steele-MacInnis, M., Ridley, J., Lecumberri-Sánchez, P., Schlegel, T.U., and Heinrich, C.A., 2016, Application of low-temperature microthermometric data for interpreting multicomponent fluid inclusion compositions: *Earth-Science Reviews*, v. 159, p. 14-35.
- Steinberger, I., Hinks, D., Driesner, T., and Heinrich, C.A., 2013, Source plutons driving porphyry copper ore formation: combining geomagnetic data, thermal constraints, and chemical mass balance to quantify the magma chamber beneath the Bingham Canyon deposit: *Economic Geology*, v. 108, p. 605-624.
- Stephens, J.D., and Bray, E., 1973, Occurrence and infrared analysis of unusual zeolitic minerals from Bingham, Utah: *The Mineralogical Record*, v. 4, p. 67-72.
- Sternier, S.M., and Bodnar, R.J., 1989, Synthetic fluid inclusions - VII. Re-equilibration of fluid inclusions in quartz during laboratory-simulated metamorphic burial and uplift: *Journal of Metamorphic Geology*, v. 1989, p. 243-260.

- Taylor, B.E., and O'Neil, J.R., 1977, Stable isotope studies of metasomatic Ca-Fe-al-Si skarns and associated metamorphic and igneous rocks, Osgood Mountains, Nevada: Contributions to Mineralogy and Petrology, v. 63, p. 1-49.
- Tooker, E.W., 1971, Regional structure control of ore deposits, Bingham Canyon mining district, Utah, U.S.A.: Geological Society of Japan, Special Issue no. 3, p. 76-81.
- van Dongen, M., Weinberg, R.F., Tomkins, A.G., Armstrong, R.A., and Woodhead, J.D., 2010, Recycling of Proterozoic crust in Pleistocene juvenile magma and rapid formation of the Ok Tedi porphyry Cu-Au deposit, Papua New Guinea: Lithos, v. 114, p. 282-292.
- Vogel, T., Cambray, F.N., Feher, L., Constenius, K., and Team, W.R., 1997, Petrochemistry and emplacement history of the Wasatch igneous belt, in John, D.A., and Ballantyne, G.H., eds., Geology and ore deposits of the Oquirrh and Wasatch Mountains, Utah: Society of Economic Geologists, Guidebook Series, v. 29, p. 35-46.
- von Quadt, A., Erni, M., Martinek, K., Moll, M., Peytcheva, I., and Heinrich, C.A., 2011, Zircon crystallization and the lifetimes of ore-forming magmatic-hydrothermal systems: Geology, v. 39, p. 731-734.
- Weis, P., Driesner, T., and Heinrich, C.A., 2012, Porphyry-copper ore shells form at stable pressure-temperature fronts within dynamic fluid plumes: Science, v. 338, p. 1613-1616.
- Welsh, J.E., and James, A.H., 1961, Pennsylvanian and Permian stratigraphy of the central Oquirrh Mountains, in Cook, D.R., ed., Geology of the Bingham mining district and northern Oquirrh Mountains, Utah Geological Survey, Guidebook to the Geology of Utah, v. 16, p. 1-16.
- Whitney, D.L., and Evans, B.W., 2010, Abbreviations for names of rock-forming minerals: American Mineralogist, v. 95, p. 185-187.
- Winchell, A.N., 1924, Petrographic studies of limestone alterations at Bingham: Transactions of the American Institute of Mining and Metallurgical Engineers, v. 70, p. 884-903.
- Zajacz, Z., Hanley, J.J., Heinrich, C.A., Halter, W.E., and Guillong, M., 2009, Diffusive reequilibration of quartz-hosted silicate melt and fluid inclusions: Are all metal concentrations unmodified?: Geochimica et Cosmochimica Acta, v. 73, p. 3013-3027.
- Zwart, E.W., and Touret, J.L.R., 1994, Melting behavior and composition of aqueous fluid inclusions in fluorite and calcite: applications within the system H<sub>2</sub>O-CaCl<sub>2</sub>-NaCl: European Journal of Mineralogy, v. 6, p. 773-786.

## Figures

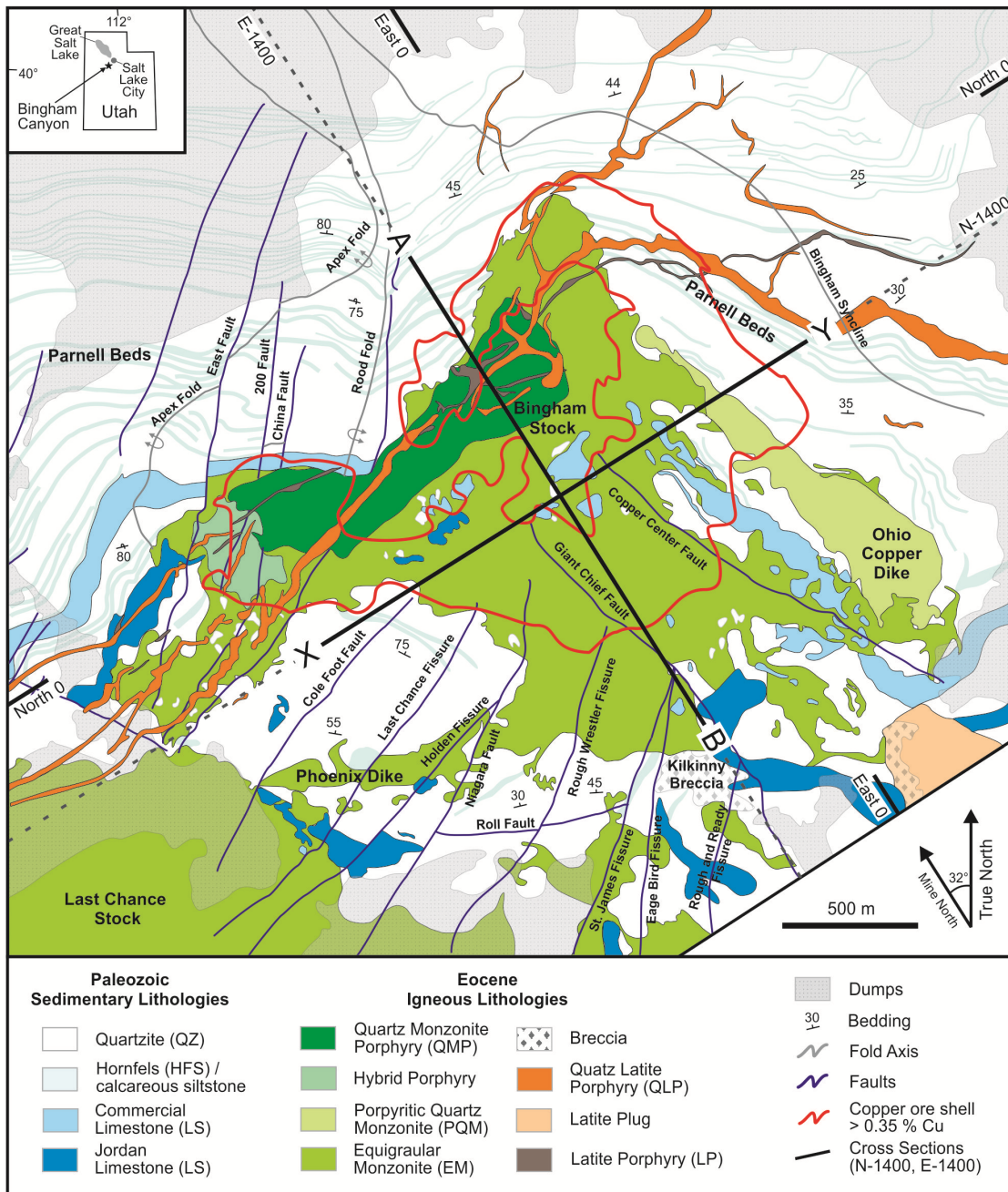


FIG. 1 Geological map of the Bingham Canyon mine area, modified after Porter et al. (2012). The principal section N-1400 (X-Y, black line) sampled for this study represents a vertical equivalent of the tilted X-Y section in Gruen et al. (2010). The section E-1400 (A-B, black line) corresponds to the section A-B in Fig. 3 of Gruen et al. (2010) and Figs. 1 and 2 in Landtwing et al. (2010).

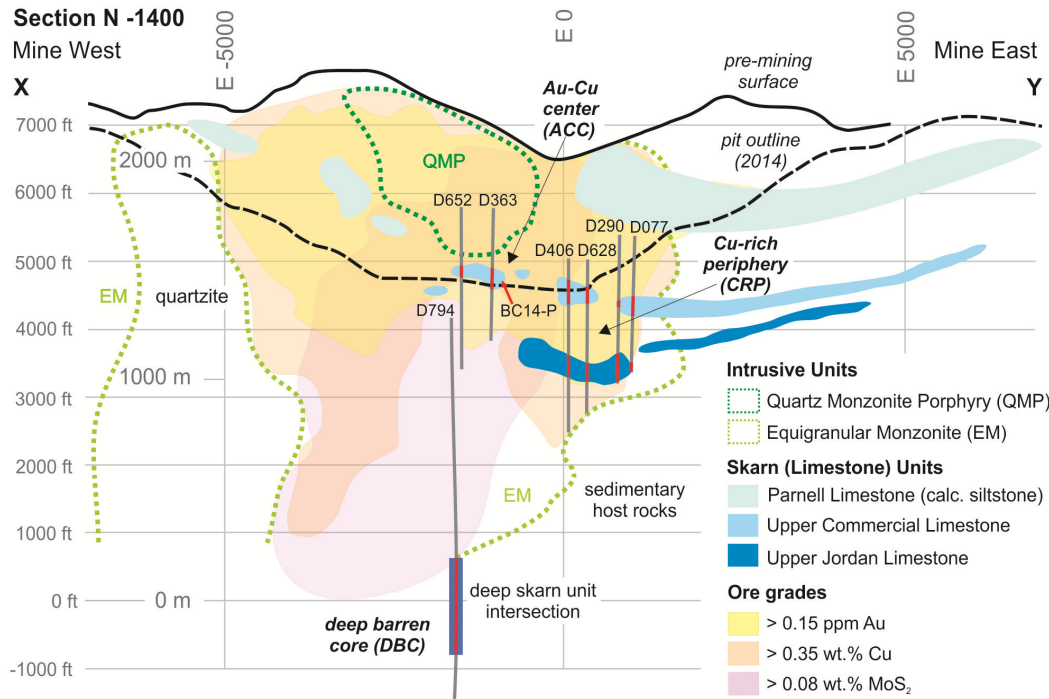


FIG. 2 Composite NNW-SSE (X-Y) section through the Bingham Canyon deposit illustrating the position of variably skarn-altered carbonate-rich sedimentary units (dismembered blue bodies, labelled as Parnell, Commercial and Jordan Limestones). Diamond drill holes (thick grey curves) indicate intersections of skarn units in red, representing the sampling locations for the present study. The core of the deposit is formed by quartz monzonite porphyry (dark green envelope), surrounded by equigranular monzonite (light green envelope), emplaced into sedimentary rocks of the Bingham Mine Formation. Grade shells for Cu, Au, and Mo are shown by transparent colors, sharply truncated at the contact to quartzite on the western side of the deposit. Note barren core including deep barren skarn within and below the inverted-cup-shaped copper orebody. Figure is based on KUCC drill core data (June 2014), oriented in KUCC mining coordinates – Mine North being rotated 32° towards East.

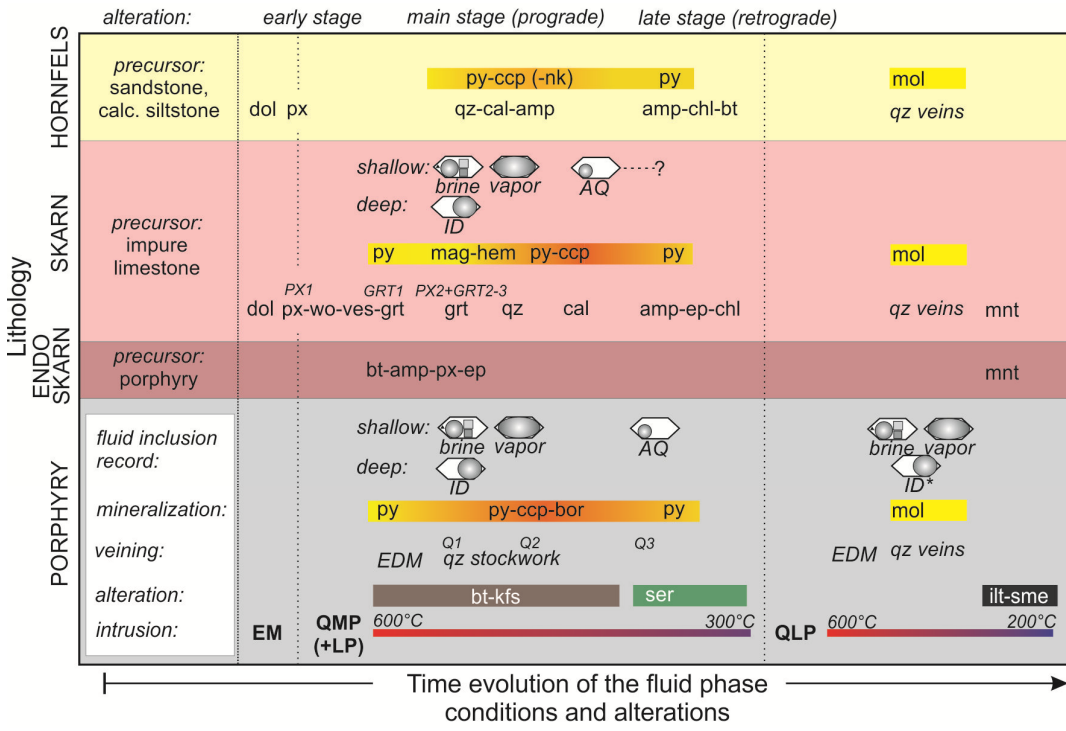


FIG. 3 Time evolution of the porphyry and skarn mineralization systems. The observations and data from porphyry published by Redmond and Einaudi (2010), Landtwing et al. (2010), and Seo et al. (2012) are compared to skarn data from this study and observations of Atkinson and Einaudi (1978), and Lanier et al. (1978). Abbreviations after Whitney and Evans (2010), including: dol = dolomite, ilt = illite, mnt = montmorillonite, ser = sericite, sme = smectite, ves = vesuvianite. The nk stands for nukundamite, an important Cu-sulfide ore mineral in quartzite lithologies (Inan and Einaudi, 2002).

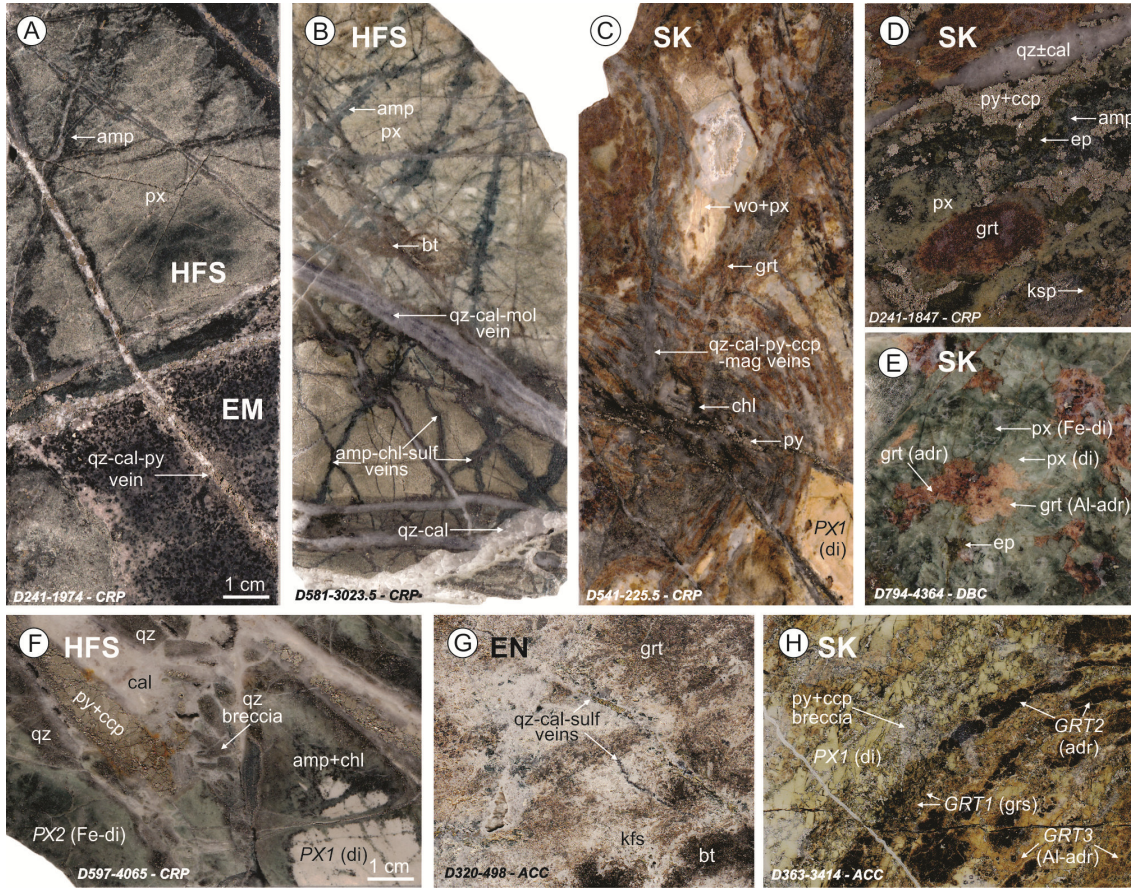
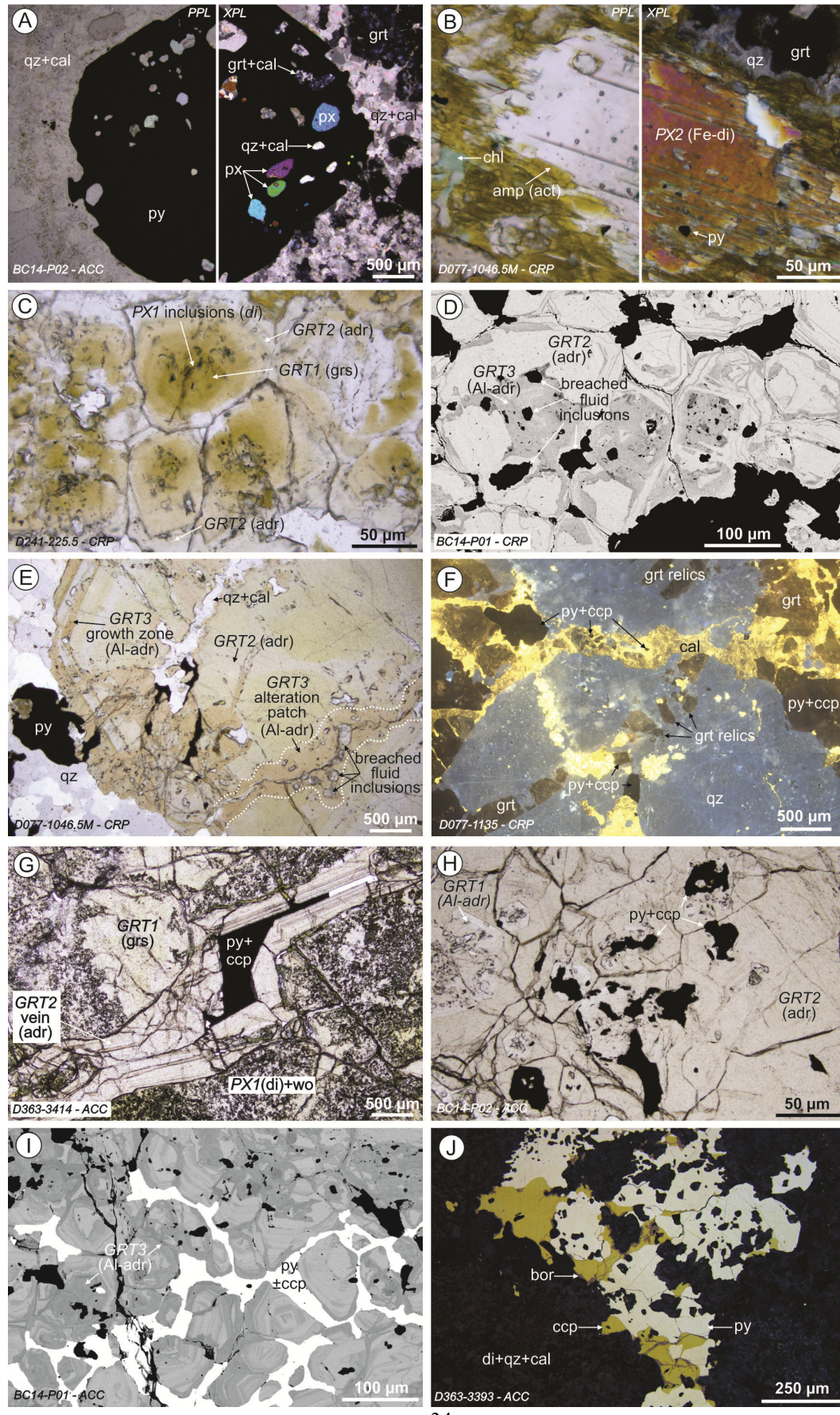
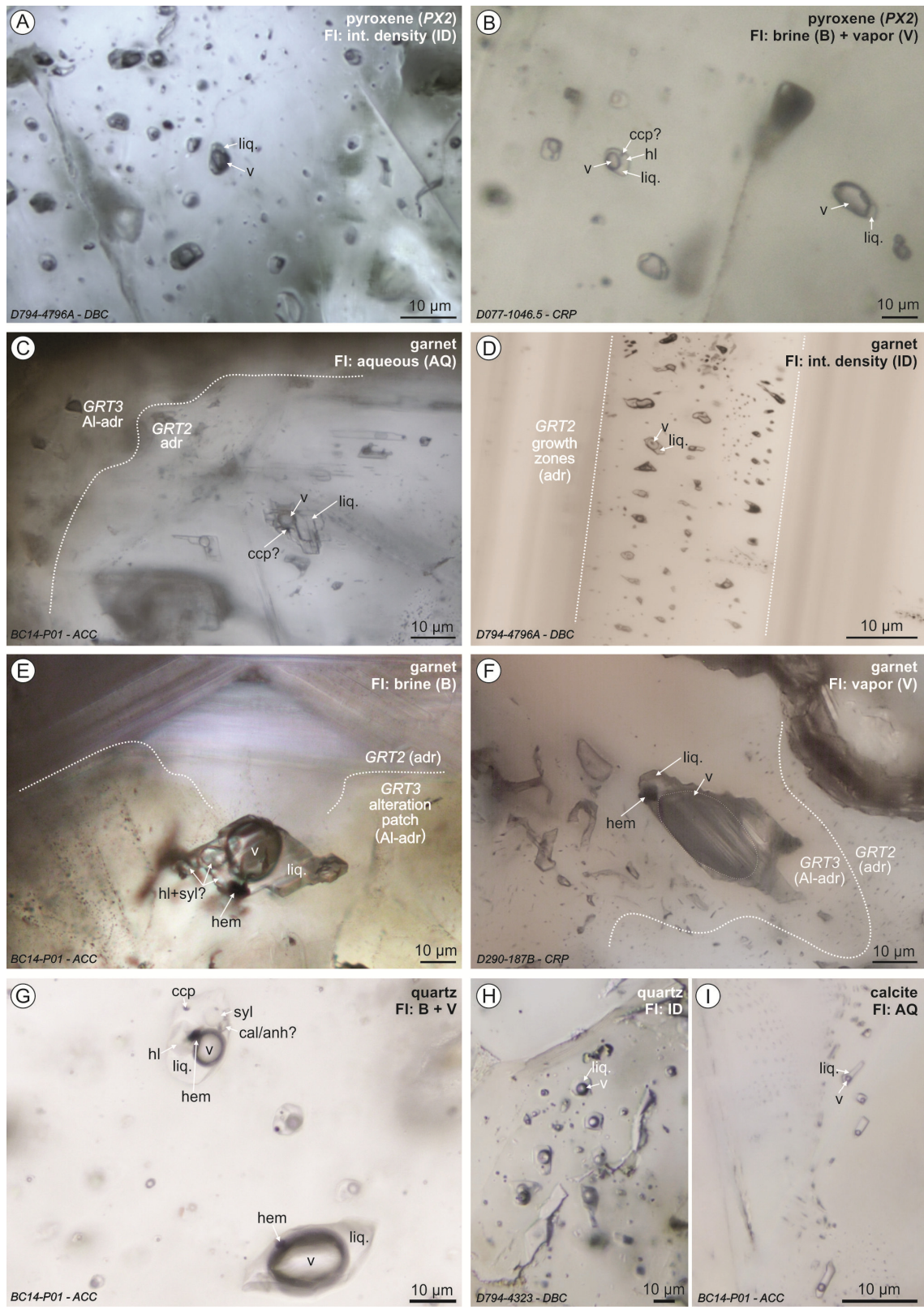


FIG. 4 Mineral relations and alteration stages: (A) sharp contact of equigranular monzonite (EM) and pyroxene hornfels (HFS) crosscut by quartz-calcite-pyrite (qz, cal, py) vein; (B) time sequence of vein formation and alteration in hornfels (px = pyroxene, amp = amphibole, bt = biotite, chl = chlorite), with molybdenite-bearing (mol) veins postdating the sulfide (ccp, py) veinlets (C) relics of early wollastonite (wo) and pyroxene selectively replaced by main stage garnet (grt) skarn (SK) and intense quartz-calcite veining with sulfides and chlorite; (D) hydrous alteration (ep = epidote) of garnet skarn with quartz-calcite-sulfide veins; (E) coarse-grained recrystallized pyroxene (diopside to ferroan diopside) and garnet (Al-free to Al-rich andradite) in deep barren skarn; (F) quartz veins in hornfels, brecciated and infilled with calcite and sulfides; (G) endoskarn (EN) with patchy garnet grading into K-feldspar (kfs) and biotite alteration; (H) fine thin cracks in pale early diopsidic pyroxene and garnet skarn filled by sulfide-only veinlets. Drill core number, depth in feet, and location of the sample is indicated in lower left corner of the photographs (ACC = Au-Cu center; CRP = Cu-rich periphery, DBC = deep barren core).



1  
2  
3  
4 FIG. 5 Microphotographs of mineral relations: (A) pyroxene ( $PX_1$ , diopside) inclusions in pyrite grain (left  
5 half of the picture in polarized light – PPL, right side in cross-polarized light – XPL); (B) pyroxene ( $PX_2$ ,  
6 ferroan diopside) partially replaced by actinolitic amphibole (act) and chlorite; (C) early garnet cores ( $GRT_1$ ,  
7 grossular) with pyroxene inclusions ( $PX_1$ ), overgrown by andraditic garnet ( $GRT_2$ ); (D) replacement of  $GRT_2$   
8 cores by a later generation of Al-rich andraditic garnet ( $GRT_3$ ) shown in back-scattered electron emission (BSE)  
9 image; (E) alteration of andradite ( $GRT_2$ ) by Al-rich andradite ( $GRT_3$ ) along fracture (stippled outline); (F) late  
10 quartz-calcite (qz, cal) veins with Cu-Fe-sulfides (py, ccp) cutting garnet skarn, shown in cathodoluminescence  
11 image; (G) early pyroxene-garnet ( $PX_1-GRT_1$ ) skarn cut by symmetrical andradite ( $GRT_2$ ) vein filled by late  
12 pyrite and minor chalcopyrite; (H) grossular ( $GRT_1$ ) cores and andradite ( $GRT_2$ ) overgrowths enclosing pyrite  
13 and chalcopyrite; (I) sulfide veinlets fracturing  $GRT_3$  garnet (BSE); (J) chalcopyrite and minor bornite replace  
14 pyrite (reflected light).

15  
16  
17  
18  
19  
20  
21  
22  
23  
24  
25  
26  
27  
28  
29  
30  
31  
32  
33  
34  
35  
36  
37  
38  
39  
40  
41  
42  
43  
44  
45  
46  
47  
48  
49  
50  
51  
52  
53  
54  
55  
56  
57  
58  
59  
60  
61  
62  
63  
64  
65



1  
2  
3  
4 FIG. 6 Fluid inclusion types in various minerals: (A) Intermediate-density (ID) two-phase inclusions in  
5 recrystallized pyroxene (*PX2*; deep skarn unit); (B) halite-bearing brine (B) and two-phase vapor (V) inclusions  
6 in recrystallized pyroxene (*PX2*); (C) aqueous (AQ) inclusions in andraditic garnet (*GRT2*); (D) primary  
7 intermediate-density (ID) inclusions in growth zone of andraditic garnet *GRT2* (deep skarn unit); (E, F) B+V  
8 inclusions in Al-rich andradite alteration patches (*GRT3*); (G) B+V inclusions in quartz; (H) ID inclusion in  
9 patchy quartz grains with interstitial calcite, (I) secondary AQ inclusions in coarse-grained calcite. Fluid and  
10 solid phases: anh = anhydrite, cal = calcite, ccp = chalcopyrite, hem = hematite, hl = halite, liq. = liquid, syl =  
11 sylvite, v = vapor bubble. For details, see text and Table 4.  
12  
13  
14  
15  
16  
17  
18  
19  
20  
21  
22  
23  
24  
25  
26  
27  
28  
29  
30  
31  
32  
33  
34  
35  
36  
37  
38  
39  
40  
41  
42  
43  
44  
45  
46  
47  
48  
49  
50  
51  
52  
53  
54  
55  
56  
57  
58  
59  
60  
61  
62  
63  
64  
65

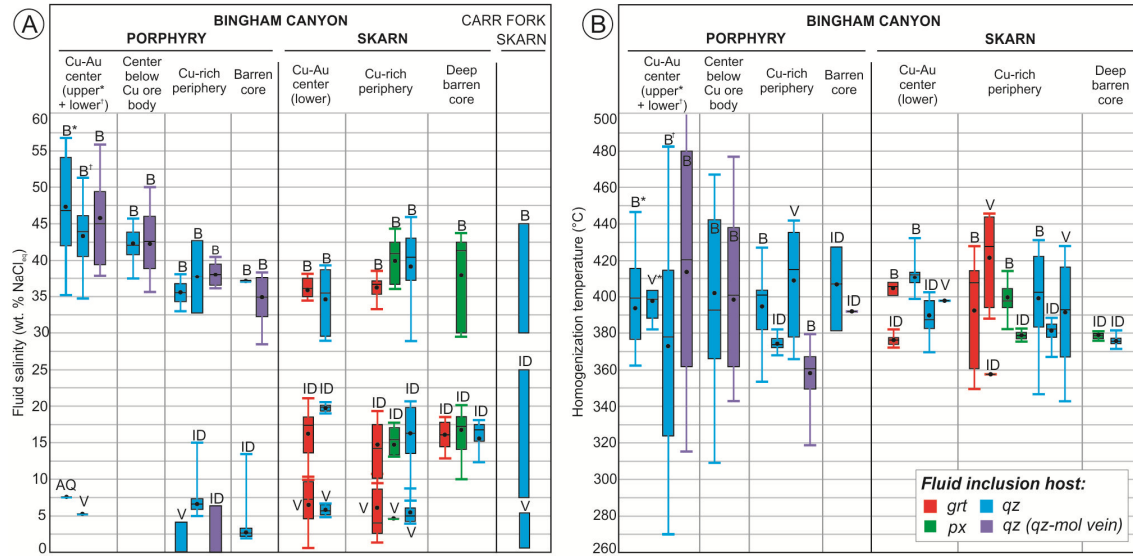


FIG. 7 Comparison of salinities (A) and homogenization temperatures (B) of fluid inclusions preserved in porphyry vs. skarn lithologies at Bingham Canyon and Carr Fork. Fluid inclusion data from porphyry part taken from Landtwing (2004), Redmond et al. (2004), Landtwing et al. (2010), and Seo et al. (2012). Data for Carr Fork skarn deposit are from Starkins (1983). Data ranges are expressed by full bars representing inner 50% percentiles with average (horizontal line) and median (black dot) and error bars extending to 90% of the total data. Presented data include microthermometry results from all single fluid inclusions in each sample type or deposit location.

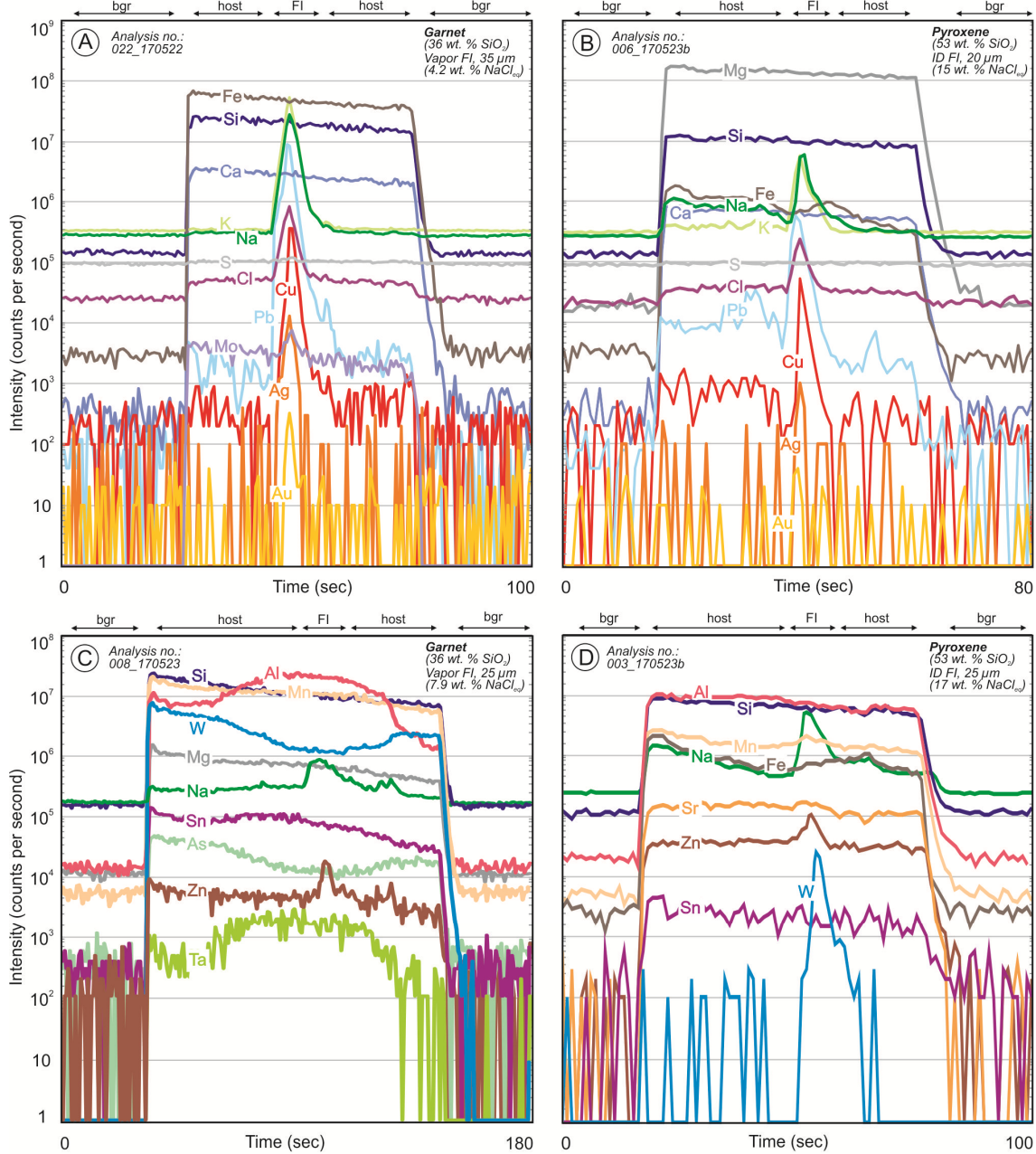


FIG. 8 Transient LA-ICP-MS signals of fluid inclusions hosted in relatively homogeneous garnet (A) and pyroxene (B), with parallel decrease of host intensities as the ablation crater narrows. Major and trace element composition and zoning of heterogeneous host minerals: garnet (C) and pyroxene (D), emphasizing the importance of correct host-mineral subtraction from fluid inclusion signals. Bgr = instrumental background, FI = fluid inclusion.

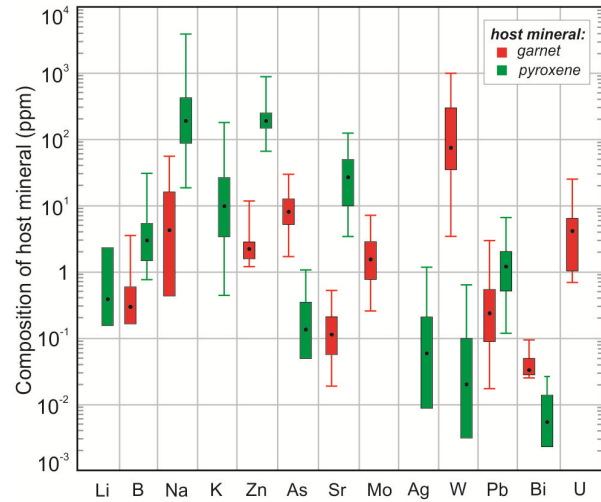


FIG. 9 Range of trace element compositions of the inclusion host minerals: garnet (red bars) and pyroxene (green). Boxes represent inner 50 % percentiles and 90% error bars from all analyzed samples, with median value indicated by the black dot.



FIG. 10 Comparison of fluid composition from three different host minerals and fluid inclusion types in skarn samples of the present study, from: (A) the Au-Cu center of the deposit; (B) the Cu-rich periphery; and (C) the deep barren core. The plotted data boxes represent 50% of the data with median (dot) and mean (black bar) values indicated. The error bars span 5–95 % of the data. Number of single fluid inclusions analyzed for each inclusion type and location is indicated in the lower right corner of each plot.

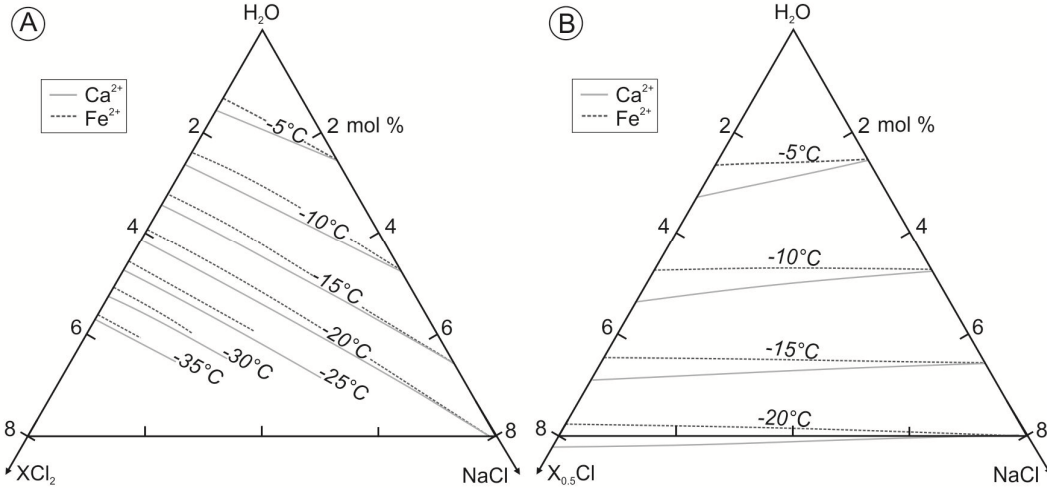


FIG. 11 Temperature contours of the ice liquidus for the  $\text{H}_2\text{O}-\text{NaCl}-\text{CaCl}_2$  and  $\text{H}_2\text{O}-\text{NaCl}-\text{FeCl}_2$  ternary systems: (A)  $\text{XCl}_2$  vs. (B)  $\text{X}_{0.5}\text{Cl}$  projection. Calculation in mol % axes using the equations of Steele-MacInnis et al. (2011) and Lecumberri-Sanchez et al. (2015) shows that the freezing-point effect of the two major divalent salts in skarn fluids are very similar.

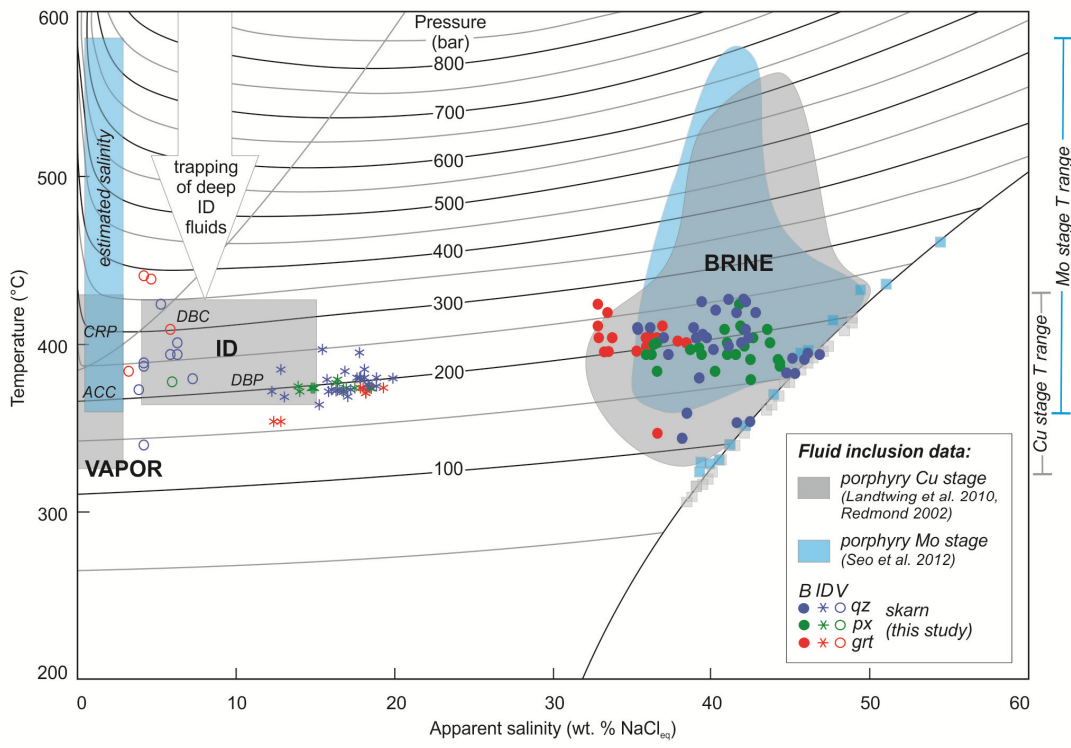


FIG. 12 Fluid inclusion salinity vs. homogenization temperature in porphyry and skarn lithologies at Bingham Canyon. The findings of this study (colored point symbols) are overlaid on previous results from the porphyry quartz stockwork (Landtwing et al., 2010; Seo et al., 2012), showing the higher salinity of intermediate-density fluid inclusions in all minerals of the skarn samples (colored stars; this study) compared to those in pre-ore stockwork veins of the barren core (grey box 'ID'; op. cit.). ACC = Au-Cu center, CRP = copper-rich periphery, DBC = deep barren core, DBP = deep barren periphery.

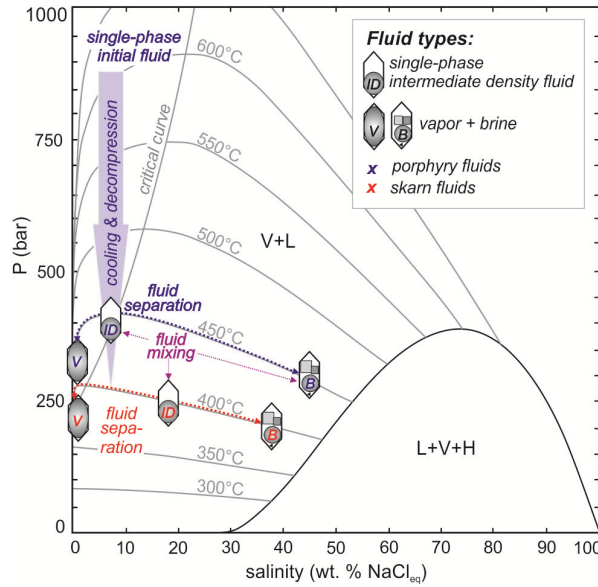
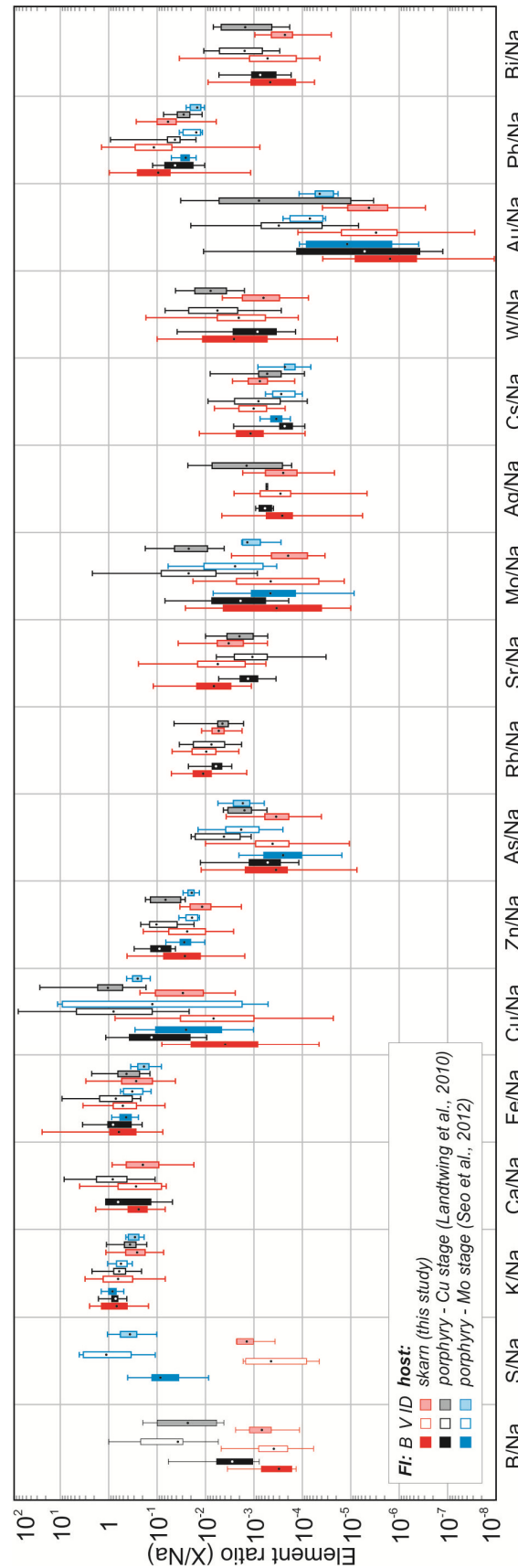


FIG. 13 Evolution of the skarn fluid composition with pressure and temperature, interpreted on the basis of the model NaCl- H<sub>2</sub>O fluid system after Driesner and Heinrich (2007). Cooling and moderate decompression of single-phase intermediate-density (ID) fluid leads to brine and vapor separation (blue; main sulfide precipitation in the porphyry stock). The resulting brine mixes with new pulses of ID fluids (purple) resulting in higher-salinity ID fluids (red, skarns).



1  
2  
3  
4 FIG. 14 Comparison of fluid inclusion compositions in skarn samples (red symbols) with those in porphyry  
5 Cu stage (black; Landtwing et al, 2010) and Mo stage quartz veins (blue; Seo et al; 2012). Brine and vapor  
6 inclusion are from the Au-Cu center and Cu-rich periphery, and ID inclusions are from the barren core. The K,  
7 Ca, and Fe to Na ratios for the skarn are derived only from quartz-hosted inclusions, while other ratios for skarn  
8 fluids include data from quartz as well as garnet. Data are presented as 50% percentile with median value  
9 indicated by the point and error bars spanning 5 to 95 % of all single fluid inclusion data. For details see text.  
10  
11  
12  
13  
14  
15  
16  
17  
18  
19  
20  
21  
22  
23  
24  
25  
26  
27  
28  
29  
30  
31  
32  
33  
34  
35  
36  
37  
38  
39  
40  
41  
42  
43  
44  
45  
46  
47  
48  
49  
50  
51  
52  
53  
54  
55  
56  
57  
58  
59  
60  
61  
62  
63  
64  
65

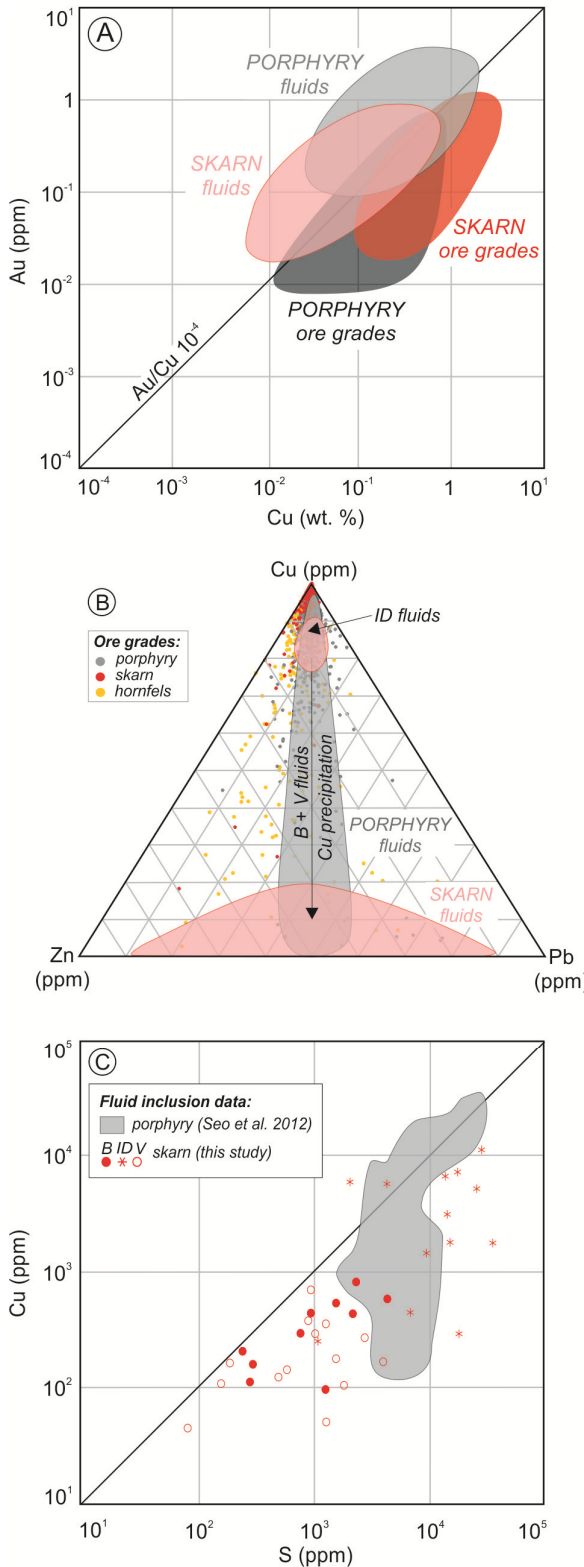


FIG. 15 (A) Au to Cu ratios and (B) Cu to Zn and Pb content of the fluids hosted by porphyry and skarn minerals compared to ore grades from the respective lithologies (porphyry ore grades include samples from EM, LP, PQM, QLP, and QMP; data from KUCC drill core database with over 500 000 assays). (C) The Cu to S ratio in the fluids preserved in porphyry vs. skarn. Fluid inclusion data from porphyry lithologies are from Seo et al. (2012).

1  
2  
3  
4  
5  
6  
7  
8  
9  
10  
11  
12  
13  
14  
15  
16  
17  
18  
19  
20  
21  
22  
23  
24  
25  
26  
27  
28  
29  
30  
31  
32  
33  
34  
35  
36  
37  
38  
39  
40  
41  
42  
43  
44  
45  
46  
47  
48  
49  
50  
51  
52  
53  
54  
55  
56  
57  
58  
59  
60  
61  
62  
63  
64  
65

## Tables

TABLE 1 Instrumental parameters for LA-ICP-MS analyses of fluid inclusions

Fluid inclusion analysis by LA-ICP-MS	
Laser type	ETH Geolas prototype 193-nm ArF-Excimer (now Coherent, Germany)
Laser energy density	6–22 J·cm <sup>-2</sup> , depending on the mineral
Laser repetition rate	10 Hz
Spot size	10–120 µm, dynamic opening with iris aperture
Ablation cell	Custom-made round, glass, 1 cm <sup>3</sup> volume
ICP-MS	Element XR, sector-field (Thermo Scientific, Bremen, Germany)
Sampler cone	Ni 1044530 (Thermo Scientific, Germany)
Skimmer cone	Nickel (H) 856-72 (AHF Analysentechnik, Germany)
Carrier gas	He, 6.0 or 5.0 grade (PanGas, Switzerland), 1.0–1.1 L·min <sup>-1</sup>
Sample gas	Ar, 6.0 grade, liquid (PanGas, Switzerland), 0.75–0.95 L·min <sup>-1</sup>
ThO <sup>+</sup> /Th <sup>+</sup> oxide ratio	< 0.25 % (on NIST SRM 610, 40 µm spot size, 10 Hz, 12 J·cm <sup>-2</sup> )
Isotopes measured	<sup>7</sup> Li, <sup>11</sup> B, <sup>23</sup> Na, <sup>24</sup> Mg, <sup>27</sup> Al, <sup>29</sup> Si, <sup>35</sup> Cl, <sup>39</sup> K, <sup>43</sup> Ca, <sup>55</sup> Mn, <sup>57</sup> Fe, <sup>65</sup> Cu, <sup>66</sup> Zn, <sup>75</sup> As, <sup>79</sup> Br, <sup>85</sup> Rb, <sup>88</sup> Sr, <sup>95</sup> Mo, <sup>107</sup> Ag, <sup>118</sup> Sn, <sup>121</sup> Sb, <sup>133</sup> Cs, <sup>137</sup> Ba, <sup>181</sup> Ta, <sup>182</sup> W, <sup>197</sup> Au, <sup>208</sup> Pb, <sup>209</sup> Bi, <sup>238</sup> U
Dwell time per isotope	20 ms for most elements, excepting: <sup>23</sup> Na, <sup>39</sup> K, <sup>34</sup> S, <sup>208</sup> Pb (50 ms); <sup>79</sup> Br, <sup>35</sup> Cl (100 ms); and <sup>197</sup> Au (200 ms)

1  
2  
3  
4 TABLE 2 Representative chemical analyses of pyroxenes. Location; ACC = Au-Cu center, CRP = Cu-rich  
5 periphery, DBC = deep barren core.

Sample	D290-91	D794-4323	D363-3414	D363-3414	D363-3414	D794-4323	D794-4364	D794-4364
	a11 pt1	a8 pt1	a4 pt2	a4 pt3	a10 pt2	a7 pt6	a2cu pt1	a3 pt1
Location	CRP	DBC	ACC	ACC	ACC	DBC	DBC	DBC
Analysis	4	82	124	125	157	80	179	181
Pyroxene type	PX1 light green	PX2 light green	PX1 pale, fine-grained	PX1 pale, fine-grained	PX1 inclusion in garnet	PX2 dark green	PX2 dark green, altered	PX2 dark green, altered
wt. %								
SiO <sub>2</sub>	54.50	54.40	54.10	54.20	53.50	52.50	51.40	51.80
TiO <sub>2</sub>	0.00	0.20	0.00	0.00	0.00	0.10	0.10	0.00
Al <sub>2</sub> O <sub>3</sub>	0.80	0.80	0.00	0.00	0.00	0.00	0.10	0.10
Cr <sub>2</sub> O <sub>3</sub>	0.00	0.00	0.00	0.00	0.00	0.00	0.00	0.00
FeO	0.60	1.90	5.10	4.60	7.60	11.20	13.80	12.80
MnO	0.00	0.30	0.40	0.60	0.20	0.90	0.40	0.40
MgO	17.80	16.50	14.80	15.20	13.60	10.70	9.90	9.90
CaO	26.10	26.20	25.50	25.60	25.30	24.40	23.90	24.50
Na <sub>2</sub> O	0.10	0.10	0.10	0.10	0.10	0.00	0.30	0.10
K <sub>2</sub> O	0.00	0.00	0.00	0.00	0.00	0.00	0.00	0.00
Total	99.90	100.40	100.00	100.30	100.30	99.80	99.90	99.60
apfu								
Si	1.973	1.975	1.998	1.992	1.989	2.002	1.969	1.989
Al <sup>[T]</sup>	0.027	0.025	0.000	0.000	0.000	0.000	0.005	0.005
Al <sup>[M]</sup>	0.007	0.009	0.000	0.000	0.000	0.000	0.000	0.000
Fe <sup>3+</sup>	0.018	0.013	0.010	0.023	0.030	0.000	0.074	0.025
Ti	0.000	0.005	0.000	0.000	0.000	0.003	0.003	0.000
Cr	0.000	0.000	0.000	0.000	0.000	0.000	0.000	0.000
Mg	0.960	0.893	0.815	0.833	0.754	0.608	0.565	0.567
Fe <sup>2+</sup>	0.000	0.045	0.147	0.118	0.207	0.357	0.358	0.386
Mn	0.000	0.009	0.013	0.019	0.006	0.029	0.013	0.013
Mg <sup>2+</sup>	0.000	0.000	0.000	0.000	0.000	0.000	0.000	0.000
Fe <sup>2+</sup>	0.000	0.000	0.000	0.000	0.000	0.000	0.010	0.000
Mn	0.000	0.000	0.000	0.000	0.000	0.000	0.000	0.000
Ca	1.012	1.019	1.009	1.008	1.008	0.997	0.981	1.008
Na	0.007	0.007	0.007	0.007	0.007	0.000	0.022	0.007
O	6.000	6.000	6.000	6.000	6.000	6.000	6.000	6.000
Mg/(Mg+Fe <sup>tot</sup> )	0.981	0.939	0.838	0.855	0.761	0.630	0.561	0.580

1  
2  
3  
4 TABLE 3 Representative chemical analyses of garnets. Location: ACC = Au-Cu center, CRP = Cu-rich  
5 periphery, DBC = deep barren core.

Sample	D794-4364	D794-4364	D794-4364	D077-1046.5	D363-3414	D077-1046.5	D363-3414	D363-3414
Location	DBC	DBC	DBC	CRP	CRP	CRP	ACC	ACC
Analysis	204	199	201	144	162	141	109	166
Garnet type	<i>GRT1</i> pink, old core	<i>GRT1</i> pink, core relict	<i>GRT1</i> pink, rim relict	<i>GRT2</i> red, growth zone	<i>GRT2</i> red, growth zone	<i>GRT3</i> orange, alteration patch	<i>GRT3</i> orange, alteration patch	<i>GRT2</i> red, anisotropic, vein
wt. %								
SiO <sub>2</sub>	38.60	37.10	36.30	35.20	35.40	35.30	35.90	34.80
TiO <sub>2</sub>	0.10	0.10	0.10	0.10	0.00	0.50	0.00	0.00
Al <sub>2</sub> O <sub>3</sub>	16.80	10.90	6.90	0.10	1.40	2.70	4.30	0.00
Cr <sub>2</sub> O <sub>3</sub>	0.00	0.00	0.00	0.00	0.00	0.10	0.00	0.00
Fe <sub>2</sub> O <sub>3</sub>	7.20	15.67	21.56	31.56	29.78	29.45	25.89	31.78
MnO	0.40	0.50	0.30	0.10	0.20	0.30	0.10	0.30
MgO	0.00	0.10	0.00	0.00	0.10	0.00	0.00	0.00
CaO	36.60	35.30	34.30	32.80	33.20	32.10	33.80	32.70
Na <sub>2</sub> O	0.00	0.10	0.10	0.00	0.00	0.10	0.00	0.00
K <sub>2</sub> O	0.00	0.00	0.00	0.00	0.00	0.00	0.00	0.00
Total	99.70	99.77	99.56	99.86	100.08	100.55	99.99	99.58
<i>apfu</i>								
Si	2.976	2.972	2.976	2.973	2.952	2.906	2.950	2.939
Ti	0.006	0.006	0.006	0.006	0.000	0.031	0.000	0.000
Al	1.527	1.029	0.667	0.010	0.138	0.262	0.416	0.000
Cr	0.000	0.000	0.000	0.000	0.000	0.007	0.000	0.000
Fe <sup>3+</sup>	0.464	0.945	1.330	1.984	1.862	1.701	1.584	2.000
Fe <sup>2+</sup>	0.000	0.000	0.000	0.022	0.007	0.124	0.017	0.020
Mn	0.026	0.034	0.021	0.007	0.014	0.021	0.007	0.021
Mg	0.000	0.012	0.000	0.000	0.012	0.000	0.000	0.000
Ca	3.024	3.030	3.013	2.968	2.967	2.832	2.976	2.959
Na	0.000	0.016	0.016	0.000	0.000	0.016	0.000	0.000
K	0.000	0.000	0.000	0.000	0.000	0.000	0.000	0.000
O	11.952	12.000	12.000	11.945	11.905	11.813	11.900	11.878
OH	0.095	0.112	0.097	0.110	0.191	0.375	0.201	0.245
Endmembers (mol. %)								
adr	23.21	47.23	66.49	98.93	93.12	85.03	79.18	98.63
grs	77.58	53.77	33.93	0.00	5.77	9.36	20.01	0.00
alm	0.00	0.00	0.00	0.73	0.22	4.13	0.58	0.06

1  
2  
3  
4 TABLE 4 Summary of fluid inclusion types and physico-chemical characteristics. Inclusions types: primary  
5 (P), pseudosecondary (PS), and secondary (S); Th\* = critical homogenization. For details see text.

Fluid inclusion type	Vapor (vol. %)	Daughter phases	Host	Relation	Salinity (wt.% NaCl <sub>eq</sub> )	Th (°C)
aqueous (AQ)	~ 20	cal/anh, ± hem	<i>GRT2</i>	PS	3.5–17.8	n.d.
	< 20		<i>CAL</i>	S	-	n.d.
Intermediate-density (ID)	~ 50	± CCP, hem?	<i>PX2</i>	P?	12.3–20.1	373–380*
	~ 50	± hem	<i>GRT2</i>	P	9.6–18.6	355–375*
	~ 50	± CCP, hem, cal/ahn	<i>QZ</i>	P?	7.5–20.6	369–395*
vapor (V)	> 70	± cal/anh	<i>PX2</i>	S?	~ 4.5	n.d.
	> 70	± cal/anh, hem	<i>GRT3</i>	P	1.8–7.2	385–442
	> 70	± cal/anh, hem	<i>QZ</i>	P/S?	3.9–6.9	388–425
brine (B)	< 30	hl, ± hem	<i>PX2</i>	S?	36.0–42.5	380–425
	< 20	salt-rich?	<i>PX2</i>	?	> 50	n.d.
	< 30	hl, hem, CCP, ± syl, can/anh	<i>GRT3</i>	P	32.8–38.5	358–425
	< 30	hl, hem, CCP, ± syl, cal/anh	<i>QZ</i>	P/S?	37.3–42.1	348–428



Click here to access/download

**Electronic Appendix (Excel etc.)**

Appendix 1 - sampling and petrography.xlsx





Click here to access/download

**Electronic Appendix (Excel etc.)**

Appendix 2 - fluid inclusion microthermometry.xlsx





Click here to access/download

**Electronic Appendix (Excel etc.)**

Appendix 3 - LA ICP MS analytical data.xlsx

